Achieving Ultrahigh Voltage Over 100 V and Remarkable Freshwater Harvesting Based on Thermodiffusion Enhanced Hydrovoltaic Generator

*Yu Chen, Jiajun He, Chengwei Ye, and Shaochun Tang**

Evaporative hydrovoltaic generators hold significant potential for alleviating water-energy crisis, but low output voltage configurations due to the slow phase transition rate of water molecules and the intricate nature of integration limit their applications. Herein, a lotus-inspired interfacial evaporation-driven hydrovoltaic generators (IEHVG) is developed for efficient generation of water vapor and electricity from seawater instead of freshwater and achieves an ultrahigh voltage output higher than 100-volt level through forested IEHVG integration. The biomimetic hydrogel is developed with specific liquid transport channels, graphene quantum dots/MXene nanocomposites, and gradient hydrophobic interface for highly enhanced photothermal evaporation and electricity generation by mimicking the transpiration process of a "stems-leaves of lotus". The synergistic thermodiffusion effect leads to the output power density of IEHVG reaches up to 45.6 μW cm^{-2} and can power electronic devices or charge commercial supercapacitors. The freshwater-electricity cogeneration integrated system consisting of 192 IEHVG units can harvest a record-breaking voltage reaching 105 V and a high freshwater harvesting rate up to 2.0 L m^{-2} h^{-1} from seawater in a well-lit outdoor area. This work demonstrates that IEHVG offers a novel concept for modular freshwater and high-voltage power sources access on offshore work platforms.

1. Introduction

Water evaporation, governed by dynamic mass and heat transfer processes, holds great potential for alleviating the water-energy crisis via harnessing the enormous energy flows.[1–3] It was demonstrated that the water molecules natural evaporation within a porous carbon black membrane can generate sustainable and considerable electric energy.[4] Specifically, the pressure increase that occurs as water molecules traverse narrow capillary channels formed by materials with charged surfaces, inducing ionic motion within the double electric layer (EDL) of the nanochannel walls generates electrical potential and current.[5–7] Hydrovoltaic generators (HVGs) were developed through adjusting the intrinsic characteristics of the materials, such as surface charge density and solid–liquid interfacial interactions. Most reports focused on streaming potential generated by traditional thermal evaporation of freshwater based on charged materials.[8–15] Recently a new technique was proposed to contribute electrical energy through the coupling of evaporating molecules with materials at the solid–liquid–gas three-phase interface.[16,17] However, the slow ambient heat replenishment imposes limitations on the vaporization and flow rate of water, restricting the output performance of HVGs, in particular, a trade-off is formed between the electricity generation and the freshwater consumption.

Solar-driven localized temperature enhancement strategy offers distinct advantages in enhancing water evaporation and flow rate via concentrating solar endotherm at the air–liquid interface, and have been identified as a green and sustainable method for desalination, wastewater purification, and power generation.[18–20] Interfacial evaporation-driven HVGs (IEHVG) mainly include photothermal interface, water transport channel, and two-electrode system, which enables a directional streaming potential generation between the two electrodes through interfacial water vapor generation.[21] Water cycle concepts that adopt IEHVG can harvest clean water vapor from the ocean and have the potential to extract streaming potential energy from the water vaporization process. Unfortunately, the thermodiffusion effect that accompanies the interfacial heating process in conventional IEHVGs inducing the movement of hydrated ions and salt ions in the direction opposite to the streaming potential have long been neglected,[22,23] which can interfere with the electrical potential enhancement of IEHVG. Therefore, in order to harvest efficient electricity and high freshwater production from seawater, the water transport and ion convection pathways of IEHVG systems are required to be rationally regulated.

Y. Chen, J. He, C. Ye, S. Tang
National Laboratory of Solid State Microstructures
Collaborative Innovation Center of Advanced Microstructures
Jiangsu Key Laboratory of Artificial Functional Materials
College of Engineering and Applied Sciences
Nanjing University
Nanjing 210093, P. R. China
E-mail: tangsc@nju.edu.cn

The ORCID identification number(s) for the author(s) of this article can be found under https://doi.org/10.1002/aenm.202400529

DOI: 10.1002/aenm.202400529

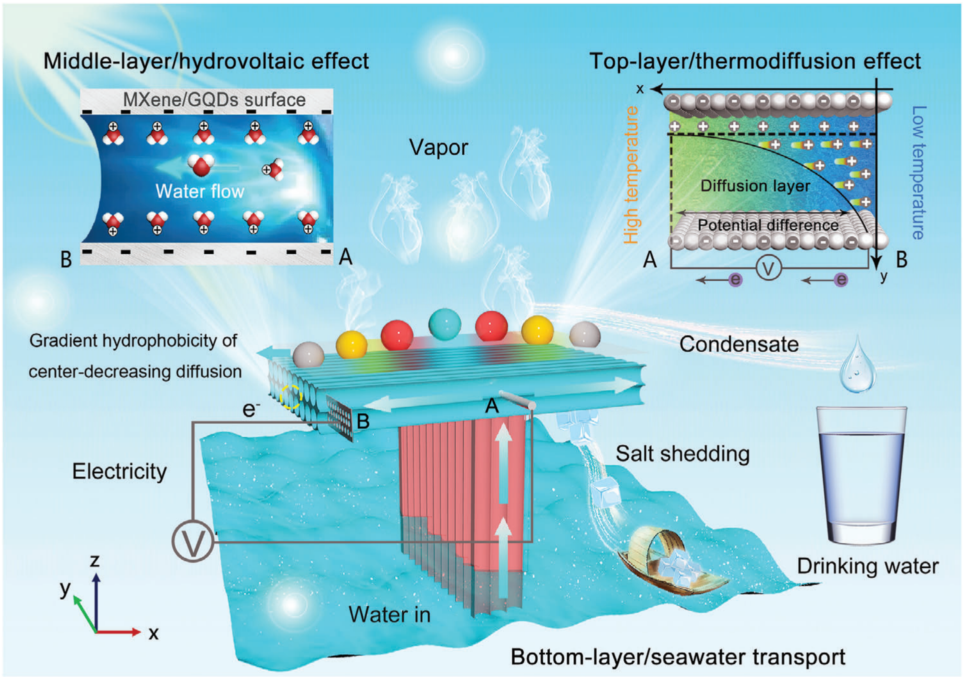

Figure 1. Schematic diagram of the working process of IEHVG. Schematic diagram of the structure and mechanism of the all-in-one IEHVG for sustained electricity output and water vapor under natural solar irradiation. Electrode selection A: Pt electrode, B: carbon nanotube (CNT) electrode.

Nature has designed well-structured water conductors in plants.[24,25] Classical "umbrella" plants such as lotus leaves, mushrooms, and so on, exhibit distinctive stems-leaves structure that integrate both lateral and longitudinal channels for water and nutrient supply. Combined with the biomimetic strategy, it is expected to overcome the conflict between thermal diffusion ion flow and streaming potential in traditional IEHVG systems, surmounting voltage output bottlenecks and concurrently obtaining high-yield freshwater resources. Nevertheless, in practical applications, the electrical output of IEHVG is also strongly influenced by factors such as solar intensity, ion concentration, EDL effect, conductivity, ambient temperature, humidity, wind, and salt resistance.[10,26–32] Integrating the limited coupling of these multiple factors complicates the integration and scaling up of biomimetic IEHVGs, resulting in the difficulty of achieving volt-level output voltage, which makes modular freshwater access and grid-connected power generation in outdoor platforms remains a great challenge so far.

In this work, inspired by stems-leaves structures of lotus and forest transpiration systems, we developed a scalable and high-efficiency IEHVG that can be easily integrated and scaled up to achieve ultrahigh voltage outputs in excess of 105 V and a freshwater generation rate of 2.0 L m^{-2} h^{-1} from seawater in well-lit outdoor area, which was the best value reported so far for modular freshwater-electricity cogeneration. Benefitting from customized water transport channels, efficient photothermal effects, and synergistic thermodiffusion effects, an IEHVG unit can achieve a high power density of 45.6 μW cm^{-2} under 1 kW m^{-2}. The optimization based on the coupling of multiple external parameters allows the integration of IEHVGs to directly drive electronic devices or charge commercial supercapacitors. This work will provide new concepts for modular freshwater and high-voltage power sources access on offshore work platforms, where scarce electrical energy and freshwater can be obtained taking advantage of the readily available seawater.

2. Results and Discussion

A schematic diagram of the working process of IEHVG is depicted in **Figure 1**. The advanced biomimetic structure and hierarchical hydrogel design provide the evaporator with excellent water transport, photothermal conversion, and power output. A transparent hydrophobic coating with a gradient from the center to the two sides was constructed on the top-layer, which generates a directional temperature gradient under solar illumination. The synergistic thermodiffusion effect enhances the flow of hydrated ions and salt ions, thereby greatly increasing the output power of the IEHVG. Simultaneously, the gradient hydrophobic design of the top-layer prevents salt ions from crystallizing and blocking the evaporation channels, ensuring stable electricity production while effectively obtaining high yields of freshwater.

Figure 2A provides the optical photographs and basic structure of the IEHVG. T-shaped monolithic design of IEHVG is inspired by the stem-and-leaf structure of lotus (inset of Figure 2A). The slender lotus stem possesses an anisotropic porous structure with longitudinal regular channels that enable directed and rapid transfer of water and nutrients. To simulate this unique structure, T-shaped hydrogel was designed using cross-linked chitosan/carboxymethyl cellulose (CS/CMC) precursors poured into a customized mold under the liquid nitrogen-assisted bidirectional ice template method (Figure S1, Supporting Information). The excellent toughness of cellulose-based materials endowed the IEHVG with exceptional flexibility and stability. The middle-layer (stem) of IEHVG will not be broken when subjected

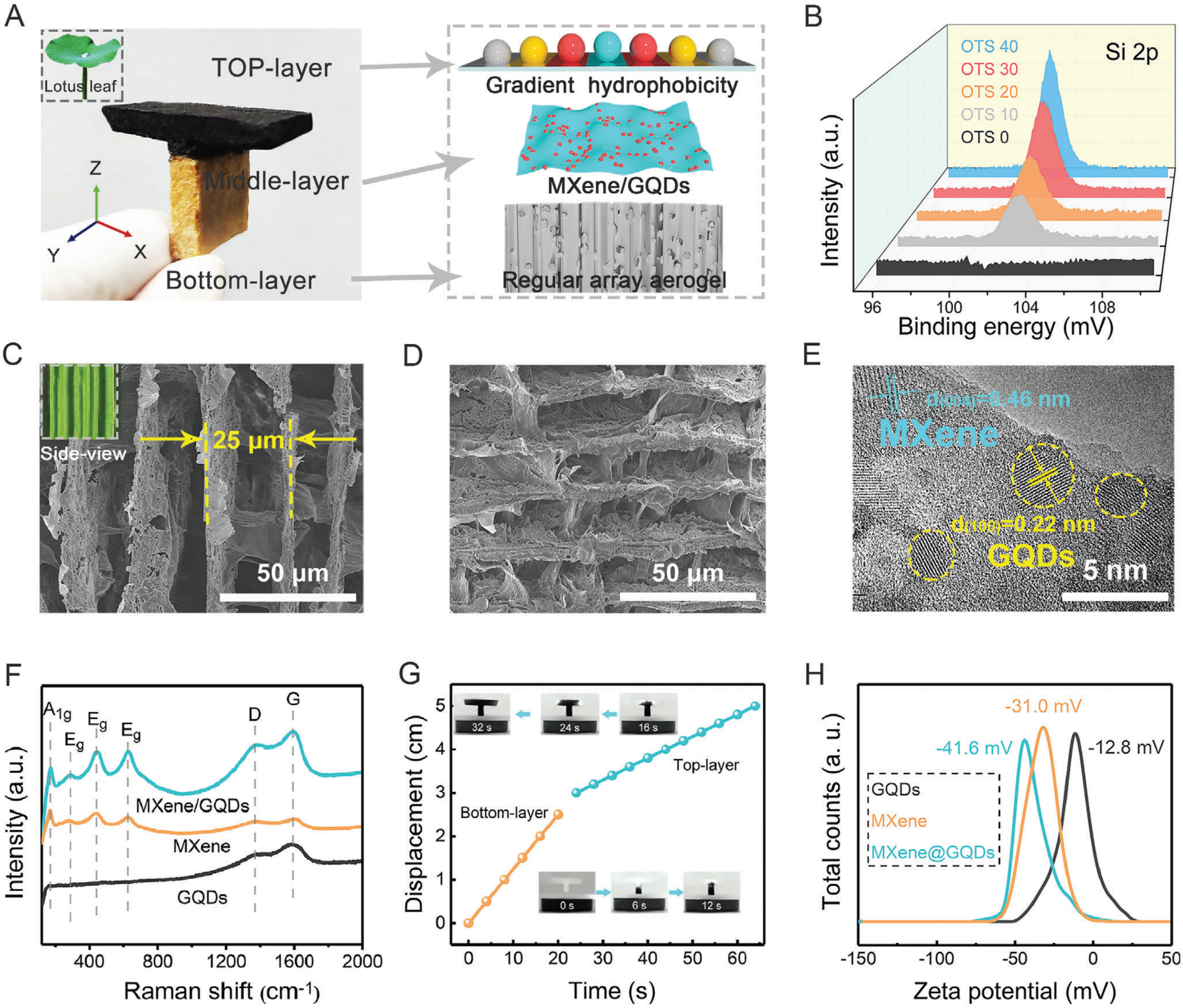

Figure 2. Structural design and characterization of IEHVG. A) Optical photograph of the fabricated IEHVG and schematic diagram of the layered functionalization, with lotus leaves in the inset. B) XPS Si 2p spectra of different regions of the top-layer OTS modification. C) Cross-sectional SEM image of the bottom-layer. D) Cross-sectional SEM image of the middle-layer. E) High-resolution TEM image of the GQDs/MXene composite on the middle-layer. F) Raman spectra of MXene, GQDs, and GQDs/MXene. G) Customized T-shaped water transport trajectory and rate of IEHVG. H) Zeta potential of MXene, GQDs, and GQDs/MXene.

to inward and outward stresses and could recover to its initial state after the stresses were relieved (Figure S2, Supporting Information). Furthermore, by fixing the bottom-layer of IEHVG, the middle-layer can lift a weight of 200 g, further demonstrating the strong binding force between the root and stem parts, which is the key to achieving a long-life and stable IEHVG for water evaporation and power generation. The bottom-layer comprises a hydrogel matrix with a regular channel structure, facilitating rapid and stable water supply during evaporation. The middle-layer is a self-assembled black graphene quantum dots (GQDs)/MXene nanocomposites on the hydrogel surface, providing the main photothermal effect and power generation. The top-layer is a transparent octadecyltrichlorosilane (OTS) gradient hydrophobic coating that forms attached covalent Si—O—Si bonds by regional spraying OTS/hexane solutions onto the T-shaped hydrogel surface. A hydrophobic gradient is generated from the center to the edges on the top-layer via controlling the number of sprays in different areas, which facilitates the formation of an effective heat distribution gradient along the direction of water diffusion to enhance the electricity output.

X-ray photoelectron spectroscopy (XPS) was employed to analyze the chemical components of the functional layers of IEHVG (Figure S3, Supporting Information). XPS spectra and high-resolution C, Ti, and O spectra confirmed the cross-linking of the hydrogel and the successful self-assembly of the GQDs/MXene.[33,34] The binding energy at 102.5 eV is assigned to Si 2p of OTS (Figure 2B), suggesting the presence of OTS on the top-layer, and the modified regions were denoted as OTS

10, OTS 20, OTS 30, and OTS 40 depending on the spraying cycle. The increase in Si 2p binding energy intensity indicates higher OTS content with increasing number of sprays. The O1s peak at 532.8 eV is attributed to CS/CMC, and its intensity decreases from OTS 10 to OTS 40 due to electron attenuation by the OTS modification (Figure S4, Supporting Information). Owing to the regional modifications with different OTS concentrations, the top-layer changes from superhydrophilic state to gradient hydrophobicity. This is confirmed by the measured water contact angles being 156.8°, 139.2°, 122.6°, and 110.4° from the center to the sides (Figure S5, Supporting Information). Such observations suggest that gradient hydrophobic surface would be the main factor for the solar-driven power generation of IEHVG, as discussed in the following.

The channels in the bottom-layer of the IEHVG, designed for rapid water transport, were created using the oriented ice template method.[35,36] Controlled by a "bottom-up" temperature gradient provided by the freezing reagent, regular columns of ice crystals form within the hydrogel precursor solution. After freeze-drying treatment, the scanning electron microscope (SEM) image of the bottom-layer reveals a regular oriented longitudinal channel structure with a diameter of ≈25 µm (Figure 2C). The customized middle-layer features horizontal regular channels achieved by rotating the freezing reagent at a 90° angle, resulting in a customized T-shaped water delivery trajectory when combined with the bottom-layer. Compared to the bottom-layer, the self-assembled GQDs/MXene exhibit numerous rough structures on the channel surface (Figure 2D), which can trap more solar to generate heat. Transmission electron microscopy (TEM) images reveal a uniform distribution of GQDs on the surface of MXene nanosheets (Figure S6, Supporting Information). High-resolution TEM (Figure 2E) shows distinct lattice stripes with d-spacing of 0.46 and 0.22 nm, corresponding to the (004) crystal plane of Ti_3C_2Tx MXene nanosheets and the (100) crystal plane of GQDs, respectively. Raman spectra demonstrates a prominent vibrational mode at ≈207 cm^{-1}, attributed to the A1g symmetric out-of-plane vibrations of Ti atoms (Figure 2F). Additionally, three modes are observed at ≈327, 416, and 618 cm^{-1}, representing the vibrations of E_g groups, including in-plane Ti, C, and surface functional group atoms, respectively. MXene/GQDs exhibit two broad bands at 1351 and 1573 cm^{-1}, corresponding to the D and G band features of graphitic carbon, confirming the coexistence of GQDs with MXene. These findings demonstrate the successful complexation of MXene and GQDs in the middle-layer. Notably, the absence of TiO_2 (150 cm^{-1}) in the Raman spectrum of GQDs/MXene serves as evidence of the excellent thermal stability and oxidation resistance of GQDs/MXene, which is crucial for long-term interfacial evaporation and power generation.

Fundamentally, the power generation capability of IEHVG is a multifactorial coupling process involving photothermal conversion, water transport, surface charge density modulation, and solid–liquid interactions between water molecules and materials.[2,28,37,38] To demonstrate the potential of IEHVG as an excellent solar-driven hydrovoltaic device, its solar energy absorption and conversion capacity were evaluated. The self-assembly of the middle-layer GQDs/MXene and the light scattering and absorption properties of the porous channels allowed IEHVG to achieve a high absorbance of 96.8% in the wavelength range of 190 to 2500 nm for photothermal conversion (Figure S7, Supporting Information). The superhydrophilic and regular porous channels of the hydrogel enable efficient water transfer from the bottom to the middle-layer through capillary force in a short time (Figure 2G), forming a continuous T-shaped water supply chain, which ensures the formation of continuous electrical signal driven by interfacial heating. The self-assembly of GQDs/MXene in the middle-layer provides excellent electrochemical activity, leading to a significant increase in surface charge density from a tiny negative charge to −17.3 nC cm^{-2} (Figure S8, Supporting Information), and a surface zeta potential of −41.6 eV (Figure 2H), which are essential for power generation.[39–41] The high conductivity of GQDs/MXene also reduces the internal resistance of the hydrogel network, contributing to power output (Figure S9, Supporting Information).

After device fabrication, the electric output performance of the IEHVG was systematically measured. Under AM 1.5 G irradiation (1 kW m^{-2}), the IEHVG was immersed in artificial seawater (3.5 wt% salinity), while two electrodes (Pt-CNT) were inserted into the middle and right parts of the middle-layer (Figure S10, Supporting Information). Note that the reasons for the choice of electrodes are discussed in detail below. The power generation performance of the IEHVG system was evaluated using a current–voltage (*I*–*V*) measurement. The device exhibits an approximately linear *I*–*V* curve between the two electrodes, with an open-circuit voltage (V_{oc}) of ≈0.8 V and a short-circuit current (I_{sc}) of ≈46.0 µA (**Figure 3A**), indicating quasi-ohmic behavior. The maximum power density is the value when the external resistance is equal to the internal resistance of the electrical generator. The maximum power density is calculated based on the maximum rectangular area within the *I*–*V* curve range (shaded area in Figure 3A) and is ≈45.6 µW cm^{-2}. The output stability of the electrical signal from the IEHVG was assessed by continuously monitoring V_{oc} and I_{sc} for 200 min under solar illumination (Figure 3B). The results showed that V_{oc}, I_{sc}, and power density reached stability within a short response time, with values comparable to the data recorded from the *I*–*V* curve measurements, indicating accurate detection and stable output of the electrical signals. Based on the experimental findings, the following working principle of the IEHVG is proposed (Figure 3C): Evaporation occurs at the interface between the middle/top-layer of the IEHVG, driving water to flow upward along the bottom-layer and continuously diffusing to both sides through the GQDs/MXene nanochannels. When the water evaporation and capillary permeation flux gradually reach equilibrium, a continuous and stable directional water flow is formed. The negatively charged nanochannels repel negatively charged ions (OH^-) but allow the passage of positively charged hydrogen ions (H^+), resulting in positive and negative charge separation and the formation of an electric potential difference. Under the action of Coulomb forces, the accumulated charges generate a diffusion current in the opposite direction of the flow, and in the steady state, the device's V_{oc}, I_{sc}, and power density reach stable values. According to streaming potential theory, the Pt electrode is negative, and the CNT electrode is positive in the IEHVG device. By repeatedly switching the connection mode between the device and the electrostatic meter, the absolute voltage value remains constant, but the signal direction is opposite, further confirming the proposed working mechanism (Figure 3D).

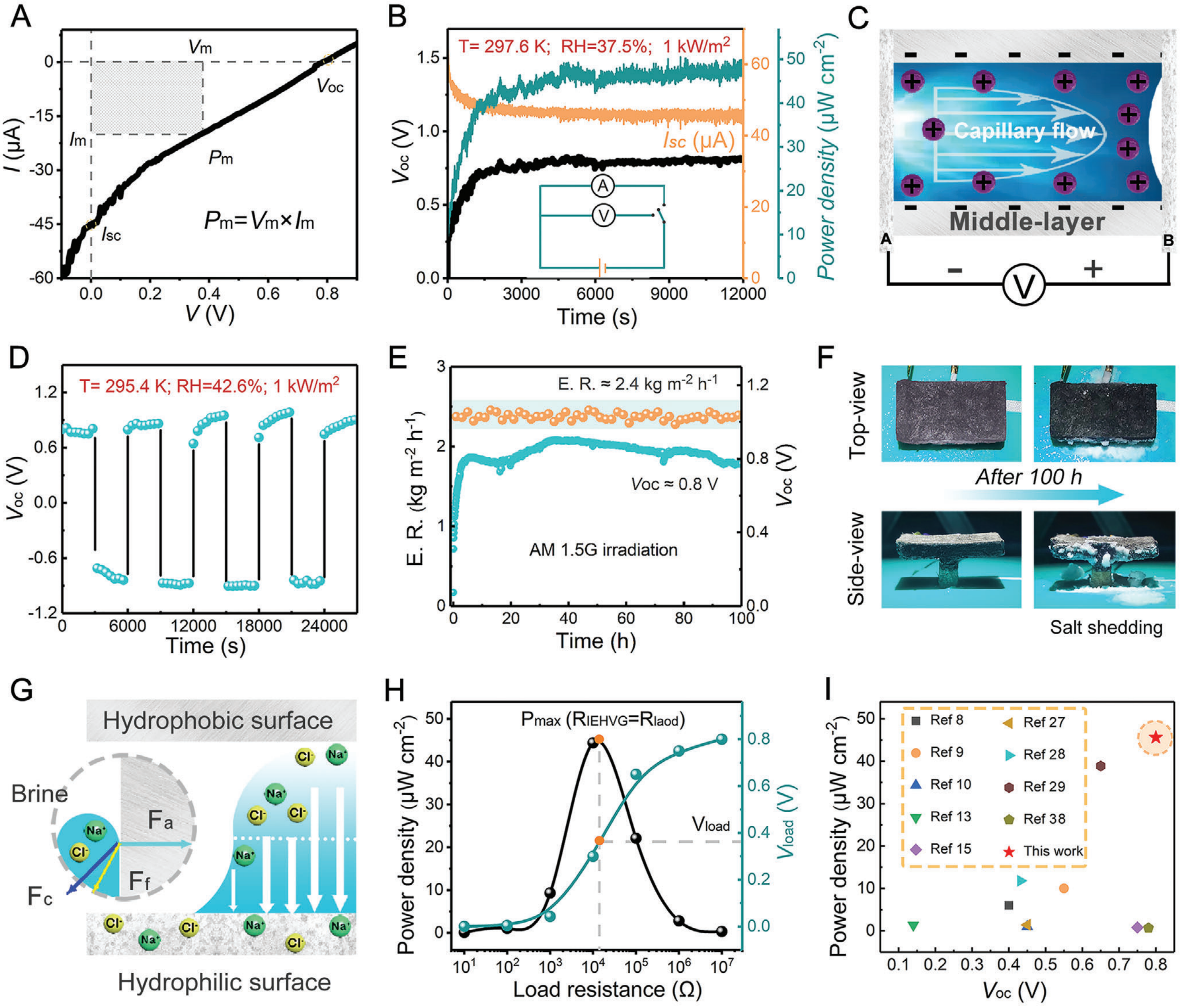

Figure 3. Power generation performance of the IEHVG. A) Current–voltage curve from the IEHVG measured by an electrochemical workstation. B) The V_{oc}, I_{sc}, and power density of the IEHVG were tested for 200 min. C) Schematic depiction of the working mechanism of the IEHVG. D) V_{oc} response versus time curve of IEHVG with switching the left and right electrodes. E) The water E. R. and V_{oc} of IEHVG for 100 h of continuous operation in seawater under 1 kW m^{-2} simulated solar irradiation. F) Optical photographs of salt crystallization at IEHVG in seawater continuously operation for 100 h. G) Mechanistic pathway of salt resistance of the IEHVG based on adhesion–cohesion interaction. H) The power density and V_{oc} values of the IEHVG with various resistances. I) Systematic performance comparison of V_{oc} and power output of various reported HVGs.

Considering the stability of the GQDs/MXene nanomaterials on IEHVG during long-term operation and the salt accumulation issue associated with the ultra-high water evaporation characteristics, a continuous 100 h stability experiment was conducted in artificial seawater (3.5 wt% salinity) under AM 1.5 irradiation. As shown in Figure 3E, the water evaporation rate (E. R.) of the IEHVG remained consistently stable at ≈2.4 kg m^{-2} h^{-1}, while the V_{oc} was also maintained at a stable value (≈0.8 V). Notably, observations during the operation of the IEHVG revealed no salt crystal deposition at the top surface (Figure 3F), while salt accumulation occurred at the sides and bottom. Figure 3G schematically explains the physical mechanism of salt rejection behind the stable operation of the IEHVG based on the adhesion–adhesion interaction between the salt particles and the top-layer.[42,43] The meniscus shape of the contact interface between the hydrophobic OTS coating and the brine is convex, indicating that the cohesive forces within the brine are greater than the adhesion forces existing between the brine and the OTS layer, resulting in the salt crystals cannot be deposited in the top-layer of IEHVG. As a comparison, the same experiment was conducted using a conventional interfacial evaporation-driven nanogenerators without OTS layer, named IENG, and it was found that salt crystals completely covered the evaporator (Figure S11, Supporting Information). The ion distribution between the electrodes of IENG tends to be homogeneous and static, thereby weakening the charge separation ability and reducing the power generation (Figure S12,

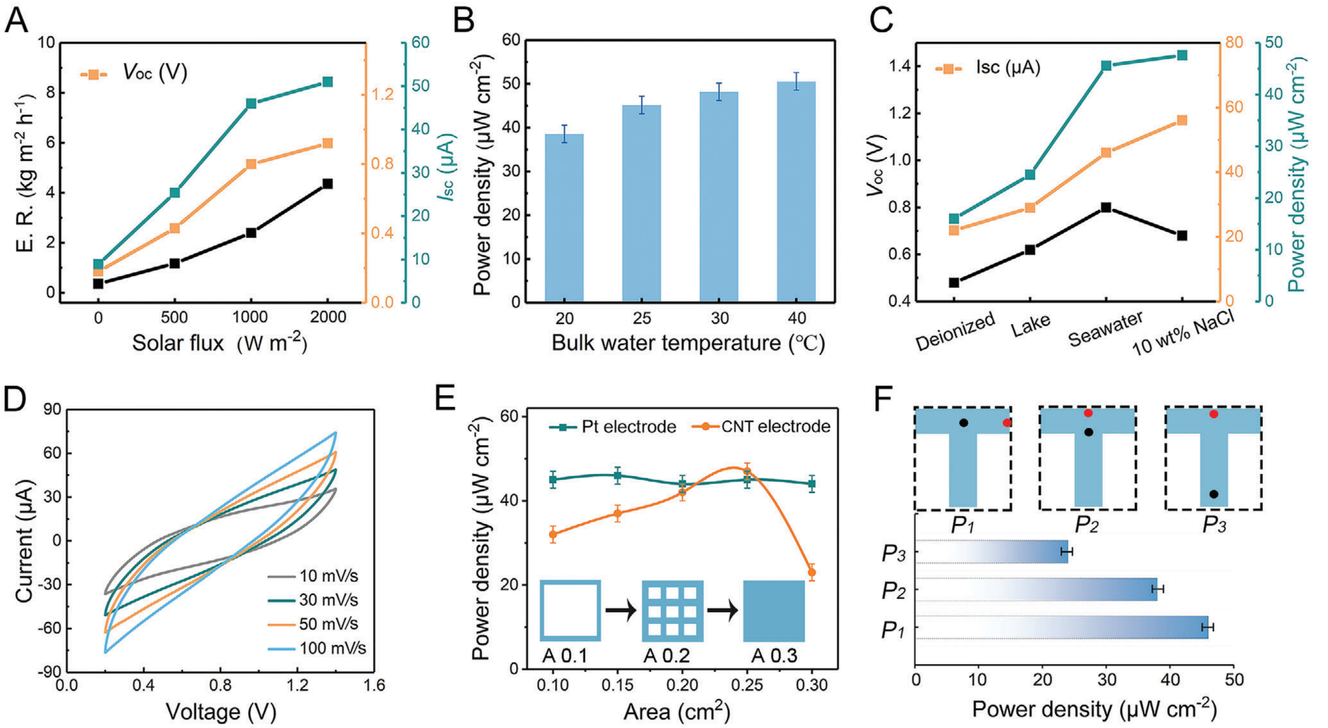

Figure 4. Analysis of influencing factors of power generation performance of the IEHVG. A) Power generation performance of the IEHVG under different solar irradiation intensities. B) The power density of IEHVG in water systems with different temperatures. C) Power generation performance of the IEHVG in different liquids. D) CV curves at scan rates of 10–100 mV s^{-1} under the irradiation of 1 kW m^{-2}. E) Power density variations by adjusting the contact area between the two electrodes and IEHVG. F) Power density variations by adjusting the relative positions of the two electrodes within IEHVG (black: Pt, red: CNT).

Supporting Information). Consequently, the unique gradient hydrophobic structure of the top-layer ensures stable operation of the evaporator in seawater. More interestingly, the salt crystals produced by the desalination process were able to be artificially collected by accumulating and shedding on the sides and bottom of the evaporator (Figure S13, Supporting Information), providing a new solution for mineral salt collection in seawater. Furthermore, the output voltage (V_{load}) and current (I_{load}) were measured at different load resistances to evaluate the practicality of the IEHVG as a power source. The results are summarized in Figure S14a (Supporting Information). The output power density was calculated from the V_{load} and I_{load} values, and it was found that the effective output power density could reach 46 μW cm^{-2} when the load resistance was ≈17.0 kΩ, with V_{load} ≈0.4 V and I_{load} ≈23.0 μA (Figure 3H; Figure S14b, Supporting Information). It is worth noting that the output power density of the IEHVG is higher than the vast majority of HVGs reported so far (Figure 3I). A systematic comparison of the power generation performance of HVGs and IEHVG with different materials is presented in Table S1 (Supporting Information). It is conceivable that the IEHVG is particularly suited to marine work platforms, where scarce electrical energy, freshwater, and mineral salts can be obtained taking advantage of the readily available seawater, thus expanding its potential applications to a wider range of scenarios.

The diverse and dynamic environmental conditions of offshore platform operations necessitate a systematic investigation of numerous objective factors influencing the electricity generation process of IEHVG to achieve optimized output performance.[28,44] Factors such as solar intensity, ambient temperature, humidity, and wind speed can impact water directional flow and evaporation. Additionally, excessive liquid ion concentration may decrease the EDL effect, while material conductivity can affect internal resistance and power output. Initially, the investigation focused on the enhanced thermodiffusion effect and evaporation rate by adjusting solar intensity. The results revealed that the power generation performance of the device increases with higher solar flux. As the light intensity increased from 0, 500, 1000, to 2000 W m^{-2}, the temperature gradient on the IEHVG surface was further amplified (Figure S15, Supporting Information), while the E. R. increased from 0.36 to 4.24 kg m^{-2} h^{-1}. Consequently, the device exhibited a V_{oc} of 0.18, 0.45, 0.80, and 0.92 V, with a corresponding linear increase in current and power density (**Figure 4**A; Figure S16, Supporting Information). It is worth noting that studying the electrical output performance of water evaporation at higher sunlight intensities holds limited significance since the maximum intensity of natural sunlight typically reaches 1000 W m^{-2}.

When considering real-world outdoor variable environments, it becomes essential to account for the interference caused by ambient temperature, humidity, and wind speed. The findings indicate that the output power of the IEHVG increases with higher water temperature (simulated ambient temperature) (Figure 4B; Figure S17, Supporting Information). Moreover, it was observed that V_{oc} did not significantly increase with increasing humidity and wind speed in the ambient experiment (Figure S18, Supporting Information). This behavior is attributed to the occurrence of the streaming potential and EDL effect between the highly hydrated hydrogel layers. Consequently, the self-generated temperature elevation resulting in an increased evaporation rate and power output is more prominent relative to the external environment. Evaporation and flow of water molecules in IEHVG are associated with the photothermal effect of the middle/top-layer exposed to sunlight. In order to investigate the water evaporation and power generation performance, IEHVG devices with middle/top-layer of different thicknesses and areas were obtained by adjusting the mold dimensions. As the thickness of the middle-layer increases, the V_{oc} of IEHVG decreases (Figure S19, Supporting Information), which is attributed to the difficulty of the synergistic thermodiffusion effect penetrating the entire device. Interestingly, the I_{sc} of the IEHVG is instead enhanced as the exposed side area increased and side evaporation intensified. Consequently, variations in the thickness of the middle-layer can significantly impact seawater evaporation and power generation performance. The effect of area changes on the power generation of the IEHVG solely originated from the decrease in power caused by the increase in diffusion internal resistance (Figure S20, Supporting Information).

The power generation performance of the IEHVG was examined under different solutions, including deionized water, lake water, artificial seawater, and 10 wt% NaCl solution, with a constant light intensity of 1 kW m^{-2}. The V_{oc} exhibited a distinct trend characterized by two processes. Initially, it increased from 0.48 V in deionized water to 0.62 V in lake water and 0.80 V in seawater (Figure 4C). However, as the ion concentration was further increased to 10 wt%, the voltage decreased to 0.68 V. During the first process, as evaporation occurs at the surface, the seawater with high ionic strength flows rapidly through the IEHVG channel. According to the Debye–Huckel theory,[45] seawater contains more charges in a "free" state, which can effectively reduce the Debye length and enhance the charge separation efficiency. On the surface of negatively charged GQDs/MXene, the staggered arrangement of nanochannels causes the overlapping of the Debye layers within the EDL,[46–48] allowing the selective transport and local accumulation of free cations (Na^+, $H3O^+$) from seawater, generating high streaming potentials and concentration Coulomb fields, thereby enhancing the electricity output. However, with the further increase in salt ion concentration, the rapidly rising Cl^- ions began to shield the surface charge of the IEHVG channel walls. Consequently, the cation-permeable selectivity of the IEHVG decreased, leading to a deterioration in voltage output. Interestingly, the I_{sc} and output power of the IEHVG system in 10 wt% NaCl solution were further enhanced by the interference of ion shielding effect, which was attributed to the increase in solution conductivity. That is, the reduction of internal resistance effectively increased the current and power density, which indicates a positive correlation between conductivity and the performance of the IEHVG, which aligns with previous studies.[12]

To evaluate the interference of current effects of heterogeneous electrodes on the IEHVG system, comparative experiments were conducted using various electrodes including Ag, Pt, Cu, and CNT. The results (Figure S21, Supporting Information) indicated that the I_{sc} of IEHVG with various electrodes were comparable to those with Pt-CNT electrodes, suggesting that the current effects on the IEHVG was negligible during the power generation process.[49,50] The oxidation–reduction and ion diffusion between PT-CNT electrodes in the IEHVG system were investigated through CV scan curves. As shown in Figure 4D, at a low scan rate of 10 mV s^{-1}, a similar rectangular CV shape indicates the absence of oxidation–reduction reactions in IEHVG, with ion transfer processes predominantly governed by the EDL diffusion. Even at a scan rate of 100 mV s^{-1}, the CV curve remains nearly rectangular without distortion. Simultaneously, it was found that only weak electrical signals (< 20 mV) could be detected at the Pt-CNT electrodes in seawater (Figure S22, Supporting Information), further demonstrating that the potential effect between Pt-CNT has minimal impact on the accuracy of the results. Therefore, the heterogeneous inter-electrode interaction of Pt-CNT is hardly involved in the electrical output performance contribution and was chosen for the clear distinction between positive and negative electrodes during integration.

Attention needs to be paid to the power generation process of IEHVG occurs on a volume unit basis, thus increasing the contact area between the electrode and the diffusion ion can enhance the electric output. As shown in Figure 4E, various power sources were customized by regulating the mesh of the two electrodes for comparison. Compared to the stable output of the Pt electrode, the contact area variation of the CNT electrode exhibits two distinct processes, with power density increasing from 32.2 μW cm^{-2} (0.1 cm^{-2}) to 45.6 μW cm^{-2} (0.25 cm^{-2}), while the voltage drops to 20.4 μW cm^{-2} at the porosity of 0%. The first process reasonably attributes the contribution to enhanced electrical output to a significant increase in the contact area. As for the CNT electrode, the streaming potential effect causes a large accumulation of positive charges near its surface. Therefore, increasing the electrode contact area is beneficial for enhancement of the power density due to the increase in the collection of positive charges. As for the Pt electrode, the ion concentration and charge distribution are homogeneous in varied area due to the rapid seawater supply from the bottom-layer, thus the devices' power density is stable even with different sizes of Pt electrode. Nevertheless, the water flow and diffused ions through the IEHVG channels are impeded when the absence of pores in the electrode membrane, resulting in the simultaneous aggregation of positive and negative ions near the electrodes, thus reducing the potential difference. The effects of different inter-electrode distances on the output performance were also investigated. It was observed that the V_{oc} and output power density of the IEHVG increased slowly with increasing inter-electrode distance, reaching the highest values when the electrodes were placed in the middle and at the edge. However, the I_{sc} of the IEHVG tended to decrease with increasing distance, likely due to the increase in internal resistance between the two electrodes (Figure S23, Supporting Information). This suggests that although the EDL covers the entire middle-layer, only the cations gathered at the contact interface of the two electrodes are involved in the final electrical generation. Moreover, three IEHVGs were designed by adjusting the electrode positions inside a given evaporator to explore the sources of improved electrical output (Figure 4F). The enhanced power output of P1 was attributed to the synergistic thermodiffusion effect, resulting in a significant improvement compared to P2. The power generation of P2 and P3 originated from the ion concentration difference

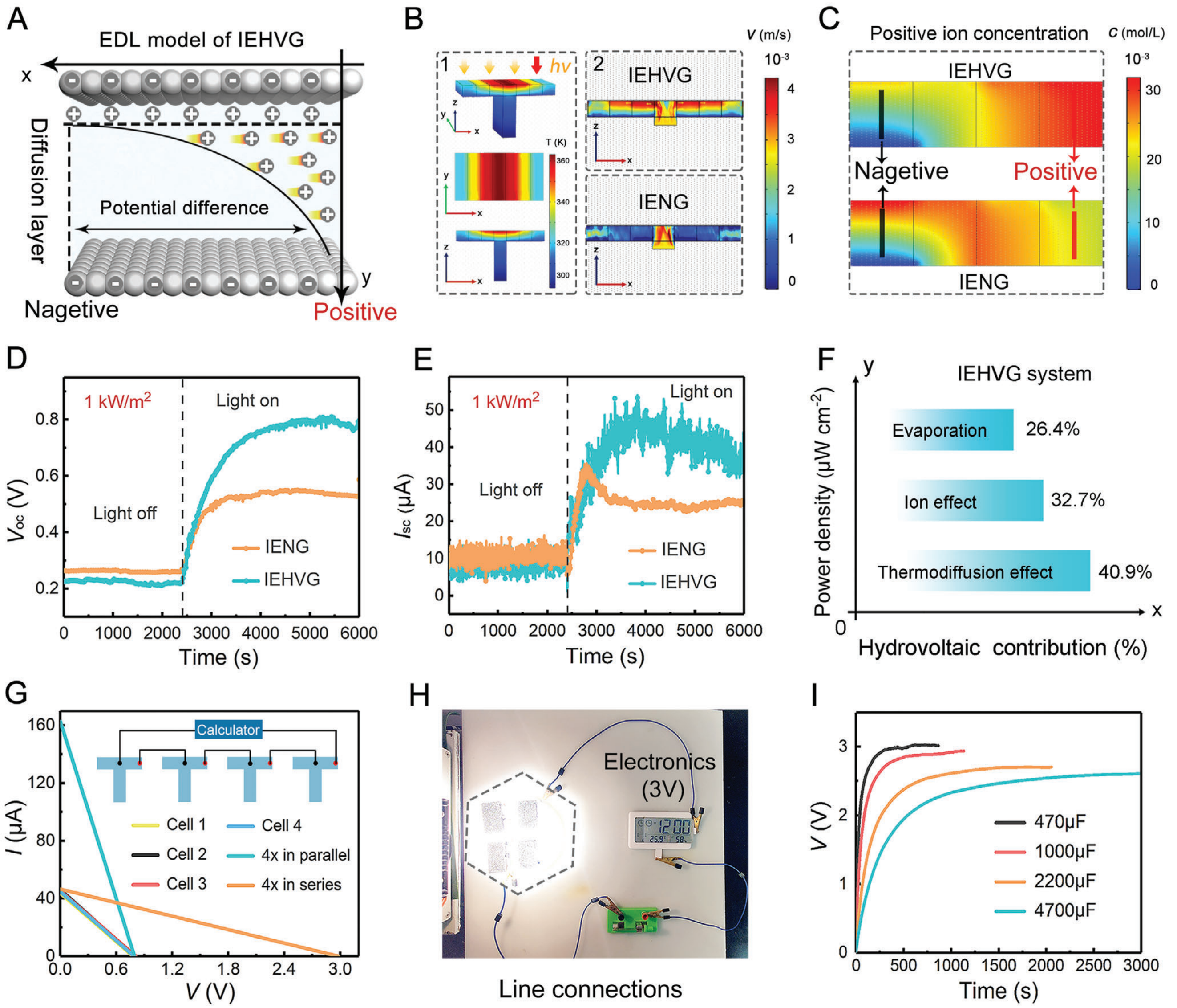

Figure 5. Proof of concept for thermodiffusion effect enhanced power generation in IEHVG. A) Schematic diagram of streaming potential generation and EDL effect in IEHVG. B) Numerical simulation of the (1) temperature distribution, (2) ion convection, and C) ionic concentration distribution of brine in IEHVG and IENG at 1 kW m^{-2}. D) Real-time V_{oc}, and E) I_{sc} changes of IEHVG and IENG before and after the irradiation of 1 kW m^{-2}. F) Numerical statistics on the contribution of hydropower generation from water evaporation energy, ionic energy, and synergistic thermal diffusion effects. G) Voltage/current output of four IEHVG units connected in series/parallel, and the V_{oc} and I_{sc} of each independent IEHVG. H) Photograph of self-powered system developed by 4x IEHVG units in series to light up the electronics (Rated voltage: 3 V). I) Real-time voltage variation of the IEHVG powering a commercial capacitor.

between the top and bottom of the middle-layer in the IEHVG. Undoubtedly, the ion concentration difference between the two electrodes in the P3 structure was greater compared to that of P2 structure. However, due to the absence of the GQDs/MXene composite material in the bottom-layer of IEHVG, selective migration and asymmetric distribution of positive charges could not be achieved. This resulted in a weaker charge separation capability for P3 compared to P2, leading to a lower power output for P3 (only half of that of P1). The structural design and thermal diffusion effect of the IEHVG clearly achieved tangible improvements compared to conventional hydroelectric devices.

Based on the above observations, we conclude here that, a synergistic volumetric potential difference was established in the middle-layer of IEHVG due to the selection of the bionic lotus stem-and-leaf structure and the customized surface thermodiffusion effect. During the phase transition from seawater to gaseous water molecules, a large number of ions such as H_3O^+, Na^+ are dissociated. The generated cations are subsequently adsorbed onto the surface of MXene/GQDs, forming an EDL (**Figure 5A**). Driven by the thermodiffusion effect, the cation transfer rate of the diffusion layer was accelerated, forming a high concentration difference and strong streaming potential at both ends of the electrode. Therefore, IEHVG exhibits a unique mechanism for interfacial evaporation power generation, driven by lateral stable ion diffusion, without being restricted by the contradictory effects of interface heat diffusion and flow potential direction, which distinguishes it from most previously reported interfacial evaporation power generation devices.

To explore the effect of gradient wetting design and synergistic thermodiffusion effect on the power generation performance of IEHVG, a conventional IENG (i.e., IEHVG without top-layer) was further constructed as a control sample for systematic evaluation. As an adjunct to the interfacial temperature enhancement strategy, the two evaporators exhibit completely different surface photothermal performance under solar illumination. The maximum surface temperature of IEHVG under 1 kW m^{-2} increases rapidly to 90.6 °C within 10 min, with an edge temperature of ≈46.8 °C, while the control sample, IENG, had a uniform temperature distribution on the top surface of ≈38.6 °C. (Figure S24, Supporting Information). COMSOL numerical simulations were employed to visualize the heat flow diffusion and ion distribution inside the IEHVG and IENG.[51,52] The simulation model was established based on the actual size, performance and experimental conditions of the IEHVG and IENG, and the details of the corresponding modeling and simulation process are described in Note S1 (Supporting Information). The photothermal effect of the IEHVG mainly occurs at the center of the evaporation interface, forming a thermal localization effect, whose temperature tends to decrease toward both ends (**Figure** 5B-1). Under the effect of temperature gradient, thermo-capillary convection occurs in the middle-layer of IEHVG, driving the hydrated and salt ions to diffuse from the center to both ends (Figure 5B-2), which is consistent with the proposed slip direction of EDL layer. Compared with IENG, the IEHVG with gradient wettability exhibits higher fluid motion rate. With the continuous photothermal evaporation process, the salt ions accumulated in the high-temperature region of the middle-layer diffuse to the low-temperature region driven by surface tension, forming a gradient-increasing concentration distribution (Figure 5C). The high flow rate and concentration difference induced by the thermodiffusion effect has a synergistic enhancement effect with the flow potential theory, it is reasonable to assume that the special thermodiffusion effect of the customized top-layer is positively correlated with its electrical output performance.

To validate the simulation results, experiments were conducted to detect the differences in the water evaporation and electrical output performance of IEHVG and IENG samples under the photothermal effect. Under natural conditions (290.1 K and 55% RH), the IENG and IEHVG detected V_{oc} signals of 0.26 and 0.22 V, respectively, primarily due to the slightly higher water evaporation rate of IENG (Figure S25, Supporting Information). When subjected to simulated solar irradiation at 1 kW m^{-2}, the IEHVG (0.8 V) showed a faster and higher response in V_{oc} compared to the IENG (0.51 V), with a steady-state increase of 0.29 V attributed to the enhanced power output resulting from the thermodiffusion effect (Figure 5D). The I_{sc} trend for both devices followed a similar pattern to V_{oc}, with the IEHVG reaching 45.7 μA and the IENG reaching 26.4 μA at steady state (Figure 5E). The above results are in line with the findings of numerical simulations and the working principle proposed based on the streaming potential theory. As a comparison, IEHVG with the top-layer of non-gradient hydrophobic coating showed only a water evaporation rate of 2.05 kg m^{-2} h^{-1} and a V_{oc} of 0.45 V, further validating the superiority of the gradient hydrophobic design (Figure S26, Supporting Information). In the case of IEHVG, efficient energy harvesting is primarily composed of two parts: the vaporization of free water molecules in seawater and the enhancement of ion flow on the EDL layer. Customized heat diffusion effects are employed to enhance water molecule movement, ion diffusion, and asymmetric ion concentration distribution, serving as a synergistic means to enhance the electrical output of IEHVG. Based on statistical analysis of the above results, Figure 5F illustrates the specific hydrovoltaic contribution rate of IEHVG. Out of the total output power of 45.6 μW cm^{-2}, ≈25.7% is attributed to free water evaporation, while the efficiency of ion flow is ≈34.2%, and the thermodiffusion effect, as a crucial means, achieves 40.7% energy enhancement. Clearly, this particular structural design is considered to offer a novel synergistic strategy for efficient energy harvesting.

Due to the special characteristics of the stem-to-leaf structure and the transverse streaming potential generation, the IEHVG can be easily integrated and extended in the plane by intertwining the "leaves". As illustrated in the inset of Figure 5G, the electrical output performance of the IEHVG system can be easily amplified by connecting the "leaves" in series or in parallel. The integration capability of the IEHVG was tested using seawater at 1 kW m^{-2}. As can be seen in Figure 5G, the total voltage value increases linearly with the number of IEHVGs connected in series (Figure S27a, Supporting Information). Similarly, the total current increases quasi-linearly with the number of IEHVGs in parallel (Figure S27b, Supporting Information). When four devices are connected in series, the V_{oc} and I_{sc} of the integrated cell reaches 3.0 V and 45.2 μA, enabling the power supply of commercial electronic devices rated at 3 V, as shown in Figure 5H, where the LED display is lit (Video S1, Supporting Information). Moreover, the generated electricity can be stored in the capacitor, the integrated IEHVG device can charge commercial capacitors of sizes (470, 1000, 2200, and 4700 μF) to a stable voltage of at least 2.5 V (Figure 5I). Theoretically, the IEHVG device can be scaled up by connecting multiple units in series and parallel to achieve higher induced voltages and currents when necessary.

Taking advantage of the scalability potential of IEHVG, large-scale outdoor freshwater-electricity cogeneration system allows for flexible design and construction. As shown in **Figure 6**A, an integrated forest-liked evaporation system consisting of a photothermal seawater evaporation section, a freshwater condensation and collection section, a salt crystal collection section, and an electrical output performance detection and utilization section. The integrated system consists of 192 IEHVG units inserted on a polystyrene foam and an effective interfacial evaporation area of ≈2000 cm^2. Under solar irradiation, the seawater was transported to the photothermal interface driven by ultra-fast liquid pumping in the bottom-layer of IEHVG, inducing huge electrical signal generation in the middle-layer and completing salt/vapor separation in the top-layer. The continuously generated water vapor gradually condenses on the sidewalls of the collector to form pure water droplets, which are collected as potable freshwater. The salt crystals produced during water evaporation are dislodged onto the polystyrene foam by gravity or external force during and are collected. The output electrical signal is monitored in real-time

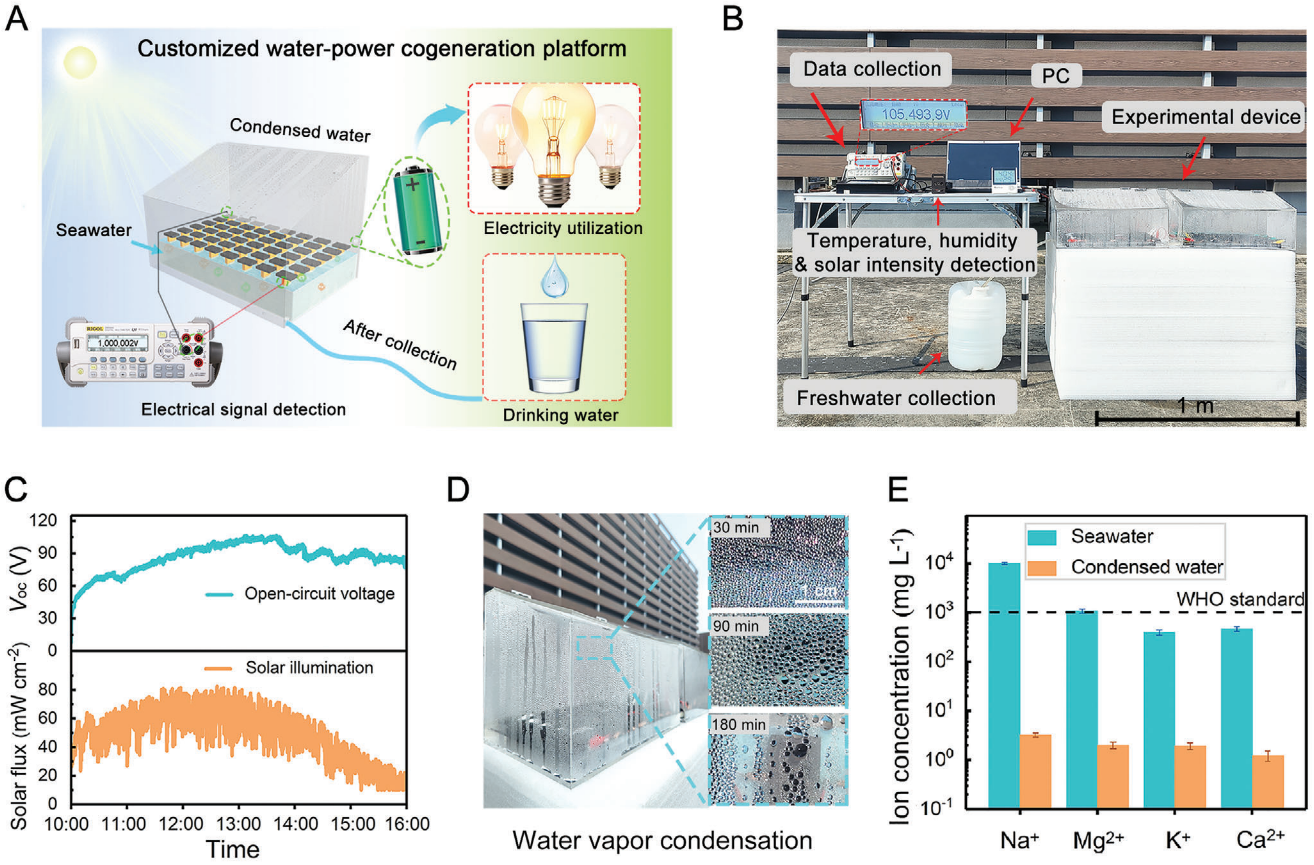

Figure 6. The integration and applications of the IEHVG. A) Self-designed outdoor freshwater-electricity cogeneration system. B) Photographs of outdoor experiments of an integrated large-scale freshwater-electricity cogeneration plant incorporating four IEHVG systems. C) Real-time evolution of light intensity (top) and open circuit voltage (bottom) of a freshwater-electricity cogeneration plant under natural solar irradiation during daytime. D) Photograph of water condensation during the water collection stage. E) Comparison of ion concentration in water before and after evaporation treatment.

by a connected multimeter and can be used to power appropriate electronic equipment.

For a practical outdoor application, a freshwater-electricity cogeneration plant was constructed on the roof of the College of Engineering and Applied Sciences (CEAS) in Nanjing, China, comprising four efficiently integrated systems, with the output devices as shown in Figure 6B. In the daytime with sufficient solar, the photothermal layer on the surface of the IEHVG module converted solar radiation into heat, driving water vapor generation at the interface and producing streaming potential for power output. As shown in Figure 6C, the ultra-high V_{oc} of ≈105.6 V was obtained when solar irradiation peaked (≈75 mW cm^{-2}), exhibiting the potential to power high-voltage devices (Video S2, Supporting Information). The water vapor released from the mixing device condensed on the surface of a transparent acrylic plate with natural convective heat transfer, and passes over an inclined surface to become water droplets to be collected (Figure 6D), with a maximum freshwater production rate of ≈2.0 L m^{-2} h^{-1} (Figure S28, Supporting Information). Testing the collected freshwater obtained from seawater revealed a nearly 100% purification rate for the main salt ions of sodium, magnesium, aluminum, and calcium, meeting world water safety standards (Figure 6E). Therefore, the IEHVG hybrid plant achieves co-production of water and electricity by synergistically harnessing solar radiation heating and water evaporation condensation, thereby addressing both the water and energy crisis. Notably, although the hybrid IEHVG device can obtain both freshwater and electricity during seawater evaporation, the primary limiting factor for water-electricity performance improvement is the daytime solar intensity. This insight has inspired further exploration of the potential application of atmospheric water production and electricity generation at night by integrating storage devices and driving the electrothermal effect.

3. Conclusion

In summary, we have successfully developed an IEHVG by simulating the stem and leaf structure of a lotus leaf, which can simultaneously generate efficient water vapor and electrical energy from seawater. The device improves the power output by hierarchical functionalization design, breaking the trade-off between thermodiffusion effect and streaming potential convective of hydrated ions in conventional HVGs. With the optimal parameters obtained by multi-parameter coupling optimization, the IEHVG achieves a freshwater yield of 2.4 kg m^{-2} h^{-1} and an output power density of 45.6 μW cm^{-2} in seawater with a light intensity of 1 kW m^{-2}. Impressively, integrating multiple IEHVGs to directly drive electronic devices or charge commercial supercapacitors in well-lit outdoor areas simultaneously achieves high voltaic output of >105 V and freshwater harvesting of 2.0 L m^{-2} h^{-1}. This work demonstrates the potential of IEHVG in developing solar-driven freshwater-electricity cogeneration systems that can be applied to future power and freshwater generation from offshore platforms.

4. Experimental Section

Materials: Chitosan (CS, Mw = 30 000), Carboxymethyl cellulose (CMC, Mw = 90 000) were purchased from Macklin, China; Glutaraldehyde (25.0–28.0%, Meryer, China); Ti_3AlC_2 powder (40 mm, 11 Technology CO., Ltd, China); lithium fluoride (LiF, 98.5%), citric acid (99%), and urea (99%) were purchase from Aladdin Biochemical Technology Co., Ltd (China); Ethanol, acetic acid, and hydrochloric acid were obtained from Sinopharm Group Chemical Reagent Co. (China); Conductive carbon nanotube ink (Alibaba, China); Porous PET film (thickness: 0.01 mm, hole diameter 0.5 mm)

Fabrication of T-Shaped Hydrogel: First, 0.3 g of chitosan and 0.3 g of CMC were added in 20 mL of 2% glacial acetic acid solution and stirred continuously for 8 h until complete dissolution. Then, 1 mL of hydrochloric acid solution (1.2 M) and 200 µL of glutaraldehyde were added to the above solution and stirred for 30 min to obtain the cross-linked CS/CMC suspension. T-shaped structure was fabricated by the ice-template-induced bidirectional freezing method. The cross-linked CS/CMC suspension was poured into a specially designed polylactide mold. Place the mold into a copper recess so that all three vertices of the T-shaped polylactide mold are in contact with the copper mold. The precursor is frozen in both directions with the aid of liquid nitrogen, and the T-shaped hydrogel matrix with customized water transport trajectory is obtained by direct lyophilization.

Fabrication of Middle-Layer of IEHVG: First, monolayer MXene and GQDs were synthesized separately using previously reported (see Note S2, Supporting Information for details). For the GQDs/MXene nanocomposites in the IEHVG middle-layer, follow this synthetic route: 30 mg of MXene nanosheets were suspended in 10 mL of ethylene glycol and 10 mL of deionized water to form a homogeneous colloidal solution. Subsequently, add 10 mg of GQDs to the Ti_3C_2Tx MXene solution and stir vigorously for 15 min to ensure thorough mixing. The resulting mixture was then transferred to a Petri dish, and the T-shaped hydrogel was immersed into the mixture 60 °C for 12 h. After that, the reaction vessel was naturally mixed with the Ti_3C_2Tx solution. After cooling the reaction to room temperature, remove the hydrogel from the mixture. Wash the hydrogel 3–5 times with a mixture of ethanol and water (1:1) to remove any residual reaction products. Finally, freeze-dry the hydrogel to obtain the bottom and middle-layer of the main body of the IEHVG. Note that to prevent the mixture from transporting to the bottom-layer of IEHVG during the reaction, let the bottom absorb saturated water before the reaction to hinder the capillary diffusion of the mixture.

Fabrication of Top-Layer of IEHVG: For top-layer, follow this synthetic route: in the initial preparation of the OTS solution, 1.0 mL of OTS and 20 µL of deionized water were added to 10 mL of n-hexane solution and sonicated in an ultrasonic cleaner for 5 min pending. The mixed solution was sprayed onto the surface of the dried T-structure hydrogel by zonation, keeping a distance of 15 cm between the sample and the spray gun. The spraying pressure was ≈0.15 MPa, and the different zones were designed as OTS 10, OTS 20, OTS 30, and OTS 40 according to the spraying cycle. The sprayed samples were then allowed to dry naturally to obtain the IEHVG sample.

Materials Characterization: XPS data were recorded using an ESCALAB 250 photoelectron spectrometer (Thermo-Fisher Scientific). SEM (Hitachi S-4800) was utilized for morphology and element analyses of the samples. TEM and HR-TEM images were obtained via a JEM-2100 microscope. Raman scattering measurements were performed by a Raman spectrometer (Renishow-inVia microscope). The water contact angles of the samples were measured by a contact angle meter (CA100D). The solar absorbance of the samples was recorded on a UV–vis–NIR spectrophotometer (Agilent Gary5000). Salt ions concentration of the seawater and purified water were measured using ICP-MS instrument (PerkinElmer NexION 300).

Measurements of Solar Steam and Power Generation Performance: The test electrodes selected in this work were platinum electrodes and CNT electrodes, where the CNT electrodes were prepared by coating the surface of porous PET film with CNT ink. In the IEHVG, the CNT electrode was placed at the edge of the middle-layer of the evaporator, while the Pt electrode was placed at the junction of the middle and bottom-layer. The photothermal evaporation experiment was conducted using CEL-HXF300-T3 xenon lamp. Temperature and infrared thermal images were detected using the infrared thermal imager (FOTRIC 320). A precision electronic balance (QUINTIX35-1CN) was used to record the instantaneous mass change of IEHVG with a resolution of 1 mg. Ambient humidity and temperature were also recorded by the Agilent data collector. All the voltage and current signals were recorded in real-time using a RIGOL 3068 multimeter, which was controlled by a LabView-based data acquisition system. To avoid any interference from static electricity, all the samples were short-circuited before testing. Humidity experiments were conducted in a constant humidity chamber, utilizing a Xiaomi humidifier to intelligently control the ambient humidity. Electrical output experiments at different wind speeds were conducted by purchasing a small fan using an anemometer to control the wind speed at 1, 2, 3, and 4 m s^{-1}.

Measurements of Outdoor Integration Platform: The outdoor experiments were conducted on the roof of the College of Engineering and Applied Sciences in Nanjing University, China, on September 18, 2023, at a temperature of 28–32 °C and an average humidity of 51%. Forty-eight IEHVG units were integrated into a customized transparent acrylic box to form an integrated platform, and condensed water vapor was simultaneously captured from four connected integrated platforms and monitored in real-time for integrated power generation performance.

Supporting Information

Supporting Information is available from the Wiley Online Library or from the author.

Acknowledgements

This work was supported by the National Key Research and Development Program of China (No. 2022YFA1602700 and 2022YFB2502104), the National Natural Science Foundation of China (22375089), the Key Research and Development Program of Jiangsu Provincial Department of Science and Technology of China (BE2020684 and BE2022332), Jiangsu Carbon Peak Carbon Neutralization Science and Technology Innovation Special Fund (BE2022605).

Conflict of Interest

The authors declare no conflict of interest.

Author Contributions

S.C.T. revised the manuscript. Y.C. conducted the synthesis, characterizations, and electrical performance measurements. J.J.H. analyzed and discussed the experimental results. C.W.Y. helped the electrical performance measurements. All the authors discussed the results and commented on the manuscript.

Data Availability Statement

Research data are not shared.

Keywords

freshwater-electricity cogeneration, hydrovoltaic generator, interfacial evaporation, thermodiffusion effect, ultrahigh voltage

Received: February 1, 2024
Revised: March 26, 2024
Published online:

---

[1] Z. H. Zhang, X. M. Li, J. Yin, Y. Xu, W. W. Fei, M. M. Xue, Q. Wang, J. X. Zhou, W. L. Guo, *Nat. Nanotechnol.* **2018**, *13*, 1109.
[2] X. F. Wang, F. R. Lin, X. Wang, S. M. Fang, J. Tan, W. C. Chu, R. Rong, J. Yin, Z. H. Zhang, Y. P. Liu, W. L. Guo, *Chem. Soc. Rev.* **2022**, *51*, 4902.
[3] B. B. Shao, Y. H. Song, Z. H. Song, Y. N. Wang, Y. S. Wang, R. Y. Liu, B. Q. Sun, *Adv. Energy Mater.* **2023**, *13*, 2204091.
[4] G. B. Xue, Y. Xu, T. P. Ding, J. Li, J. Yin, W. W. Fei, Y. Z. Cao, J. Yu, L. Y. Yuan, L. Gong, J. Chen, S. Z. Deng, J. Zhou, W. L. Guo, *Nat. Nanotechnol.* **2017**, *12*, 317.
[5] M. Heiranian, Y. Noh, N. R. AluruHeiranian, *J. Chem. Phys.* **2021**, *154*, 134703.
[6] H. Lim, M. S. Kim, Y. Cho, J. Ahn, S. Ahn, J. S. Nam, J. Bae, T. G. Yun, I.-D. Kim, *Adv. Mater.* **2023**, *32*, 2301080.
[7] L. M. Wang, W. F. Zhang, Y. Deng, *ACS Nano* **2023**, *17*, 14229.
[8] Y. S. Qin, Y. S. Wang, X. Y. Sun, Y. J. Li, H. Xu, Y. S. Tan, Y. Li, T. Song, B. Q. Sun, *Angew. Chem., Int. Ed. Engl.* **2020**, *59*, 10619.
[9] B. B. Shao, Z. H. Song, X. Chen, Y. F. Wu, Y. J. Li, C. C. Song, F. Yang, T. Song, Y. S. Wang, S.-T. Lee, B. Q. Sun, *ACS Nano* **2021**, *15*, 7472.
[10] X. M. Liu, T. Ueki, H. Y. Gao, T. L. Woodard, K. P. Nevin, T. D. Fu, S. Fu, L. Sun, D. R. Lovley, J. Yao, *Nat. Commun.* **2022**, *13*, 4369.
[11] K. Ni, B. T. Xu, Z. Q. Wang, Q. Y. Ren, W. B. Gu, B. Q. Sun, R. Y. Liu, X. H. Zhang, *Adv. Mater.* **2023**, *35*, 2305438.
[12] Q. Hu, Y. J. Ma, G. P. Ren, B. T. Zhang, S. G. Zhou, *Sci. Adv.* **2022**, *8*, eabm8047.
[13] J. Garemark, F. Ram, L. Liu, I. Sapouna, M. F. C. Ruiz, P. T. Larsson, Y. Y. Li, *Adv. Funct. Mater.* **2022**, *33*, 2208933.
[14] N. He, H. N. Wang, F. Li, B. Jiang, D. W. Tang, L. Li, *Energy Environ. Sci.* **2023**, *16*, 2494.
[15] L. B. Liu, Y. Y. Huang, Q. J. Chang, H. B. Liu, Q. Z. Gou, X. S. Tang, M. Li, J. Qiu, *Appl. Phys. Lett.* **2023**, *122*, 103903.
[16] S. M. Fang, J. D. Li, Y. Xu, C. Shen, W. L. Guo, *Joule* **2022**, *6*, 690.
[17] S. M. Fang, H. Lu, W. C. Chu, W. L. Guo, *Nano Res. Energy* **2024**, *3*, e9120108.
[18] M. M. Gao, L. L. Zhu, C. K. Peh, G. W. Ho, *Energy Environ. Sci.* **2019**, *12*, 841.
[19] C. J. Chen, Y. D. Kuang, L. B. Hu, *Joule* **2019**, *3*, 683.
[20] F. Zhao, Y. H. Guo, X. Y. Zhou, W. Shi, G. H. Yu, *Nat. Rev. Mater.* **2020**, *5*, 388.
[21] J. X. Gui, C. C. Li, Y. Cao, Z. X. Liu, Y. J. Shen, W. Huang, X. L. Tian, *Nano Energy* **2023**, *107*, 108155.
[22] C.-G. Han, X. Qian, Q. Li, B. Deng, Y. Zhu, Z. Han, W. Zhang, W. Wang, S.-P. Feng, G. Chen, W. Liu, *Science* **2020**, *368*, 1091.
[23] Z. N. Sun, W. L. Zhang, J. C. Guo, J. N. Song, X. Deng, *J. Phys. Chem. Lett.* **2021**, *12*, 12370.
[24] Y. M. Chen, S. J. Li, X. L. Li, C. T. Mei, J. J. Zheng, S. E., G. Duan, K. M. Liu, S. H. Jiang, *ACS Nano* **2021**, *15*, 20666.
[25] T. Arunkumar, H. W. Lim, D. Denkenberger, S. J. Lee, *Renewable Sustainable Energy Rev.* **2022**, *158*, 112121.
[26] B. X. Ji, N. Chen, C. X. Shao, Q. W. Liu, J. Gao, T. Xu, H. H. Cheng, L. T. Qu, *J. Mater. Chem. A* **2019**, *7*, 6766.
[27] X. Q. Huangfu, Y. Guo, S. M. Mugo, Q. Zhang, *Small* **2023**, *19*, 2207134.
[28] Z. Z. Sun, C. L. Han, S. W. Gao, Z. X. Li, M. X. Jing, H. P. Yu, Z. K. Wang, *Nat. Commun.* **2022**, *13*, 5077.
[29] J. Y. Liu, L. Y. Huang, W. J. He, X. X. Cai, Y. Wang, L. H. Zhou, Y. Yuan, *Nano Energy* **2022**, *102*, 107709.
[30] Z. B. Jiang, T. T. Yang, X. L. Lu, C. Q. Fu, Y. Zhang, K. D. Shang, J. Zhou, C. L. He, P. F. Zhu, Q.-C. He, *Nano Energy* **2023**, *108*, 108220.
[31] Z. H. Song, C. Ge, Y. H. Song, Z. W. Chen, B. B. Shao, X. R. Yuan, J. Y. Chen, D. Xu, T. Song, J. Fang, Y. S. Wang, B. Q. Sun, *Small* **2023**, *19*, e2205265.
[32] H. Y. Peng, D. Wang, S. H. Fu, *Chem. Eng. J.* **2021**, *426*, 131818.
[33] P. Chang, H. Mei, Y. Zhao, L. K. Pan, M. G. Zhang, X. Wang, L. F. Cheng, L. T. Zhang, *Adv. Sci.* **2022**, *9*, e2204086.
[34] H. Qiu, X. W. Qu, Y. J. Zhang, S. Chen, Y. Z. Shen, *Adv. Mater.* **2023**, *32*, 2302326.
[35] S. Deville, *Natl. Sci. Rev.* **2019**, *6*, 184.
[36] Y. Chen, J. Yang, D. F. Zhang, S. Z. Wang, X. H. Jia, Y. Li, D. Shao, L. Feng, H. J. Song, S. C. Tang, *J. Mater. Chem. A* **2023**, *11*, 2349.
[37] J.-S. Jang, Y. Lim, H. Shin, J. Kim, T. G. Yun, *Adv. Mater.* **2023**, *35*, 2209076.
[38] J. Tan, S. M. Fang, Z. H. Zhang, J. Yin, L. X. Li, X. Wang, W. L. Guo, *Nat. Commun.* **2023**, *13*, 3643.
[39] Q. L. Ma, Q. Y. He, P. F. Yin, H. F. Cheng, X. Y. Cui, Q. B. Yun, H. Zhang, *Adv. Mater.* **2020**, *32*, 2003720.
[40] J. Liu, J. X. Gui, W. T. Zhou, X. L. Tian, Z. X. Liu, J. Q. Wang, J. Liu, L. Yang, P. Zhang, W. Huang, J. C. Tu, Y. Cao, *Nano Energy* **2021**, *86*, 106112.
[41] L. H. Li, S. J. Feng, Y. Y. Bai, X. Q. Yang, M. Y. Liu, M. M. Hao, S. Q. Wang, Y. Wu, F. Q. Sun, Z. Liu, T. Zhang, *Nat. Commun.* **2022**, *13*, 1043.
[42] X. Chen, S. M. He, M. M. Falinski, Y. X. Wang, T. Li, S. X. Zheng, D. Y. Sun, J. Q. Dai, Y. H. Bian, X. B. Zhu, J. Y. Jiang, L. B. Hu, Z. J. Ren, *Energy Environ. Sci.* **2021**, *14*, 5347.
[43] Y. K. Tian, Y. J. Li, X. Y. Zhang, J. Jia, X. Yang, S. K. Yang, J. Y. Yu, D. Q. Wu, X. L. Wang, T. T. Gao, F. X. Li, *Adv. Funct. Mater.* **2022**, *32*, 2113258.
[44] Z. C. Wei, C. Y. Cai, Y. Z. Huang, Y. Q. Wang, Y. Fu, *Nano Energy* **2021**, *86*, 106138.
[45] M. Simoncelli, N. Ganfoud, A. Sene, M. Haefele, B. Daffos, P.-L. Taberna, M. Salanne, P. Simon, B. Rotenberg, *Phys. Rev. X* **2018**, *8*, 021024.
[46] W. Song, H. Joshi, R. Chowdhury, J. S. Najem, Y.-X. Shen, C. Lang, C. B. Henderson, Y.-M. Tu, M. Farell, M. E. Pitz, *Nat. Nanotechnol.* **2020**, *15*, 73.
[47] J. Shen, G. Liu, Y. Han, W. Jin, *Nat. Rev. Mater.* **2021**, *6*, 294.
[48] Z. Y. Wang, Y. C. Huang, T. S. Zhang, K. Q. Xu, X. L. Liu, A. R. Zhang, Y. Xu, X. Zhou, J. W. Dai, Z. N. Jiang, G. A. Zhang, H. F. Liu, B. Y. Xia, *J. Am. Chem. Soc.* **2024**, *146*, 1690.
[49] J. Yin, Z. Zhang, X. Li, J. Zhou, W. L. Guo, *Nano Lett.* **2012**, *12*, 1736.
[50] A. T. Liu, G. Zhang, A. L. Cottrill, Y. Kunai, A. Kaplan, P. Liu, V. B. Koman, M. S. Strano, *Adv. Energy Mater.* **2018**, *8*, 1802212.
[51] X. L. Lu, T. T. Yang, C. Q. Fu, Z. B. Jiang, Y. Zhang, K. D. Shang, C. L. He, J. Zhou, Q.-C. He, *Adv. Energy Mater.* **2022**, *12*, 2202634.
[52] Y. C., H. Y. Wang, J. X. Bai, T. C. He, H. H. Cheng, T. L. Guang, H. Z. Yao, L. T. Qu, *Nat. Commun.* **2022**, *13*, 6819.

ADVANCED
ENERGY
MATERIALS

Supporting Information

for *Adv. Energy Mater.*, DOI 10.1002/aenm.202400529

Achieving Ultrahigh Voltage Over 100 V and Remarkable Freshwater Harvesting Based on Thermodiffusion Enhanced Hydrovoltaic Generator

*Yu Chen, Jiajun He, Chengwei Ye and Shaochun Tang**

Supporting Information for

Achieving Ultrahigh Voltage over 100 V and Remarkable Freshwater Harvesting based on Thermodiffusion Enhanced Hydrovoltaic Generator

Yu Chen,[1] Jiajun He,[1] Chengwei Ye,[1] Shaochun Tang*, [1]

National Laboratory of Solid State Microstructures, Collaborative Innovation Center of Advanced Microstructures, Jiangsu Key Laboratory of Artificial Functional Materials, College of Engineering and Applied Sciences, Nanjing University, Nanjing 210093, P. R. China.

Corresponding authors *E-mails: tangsc@nju.edu.cn (S.C. Tang)

Brief description of what this file includes:

Figure S16. Mass change and Voc of IEHVG under different solar intensity.
Figure S17. Voc and Isc of IEHVG with different water temperature.
Figure S18. The Voc, Isc, and power density of IEHVG under different ambient humidity and wind speed.
Figure S19. The optical photographs, power generation, and water evaporation performance of IEHVGs with different thicknesses of middle-layers.
Figure S20. The optical photographs, power generation, and water evaporation performance of IEHVGs with different surface area of middle-layers.
Figure S21. Current effect testing of IEHVG.
Figure S12. The electric potential effect of the electrode in NaCl solution.
Figure S23. The output performance of IEHVGs with different inter-electrode distances.
Figure S24. IR images of IEHVG and IENG.
Figure S25. Water evaporation mass change of IEHVG and IENG.
Figure S26. Water evaporation mass loss and Voc from IEHVG with non-gradient hydrophobic coating.
Figure S27. Voltage output of the IEHVG with increasing numbers of device units in series and in parallel.
Figure S28. The evaporation rate, ambient temperature, and humidity detection for outdoor experiments.
Table S1. Comparison of the power generation performance of IEHVG with other reported HVGs.

Note S1. The numerical simulation of IEHVG and IENG

Numerical simulation was conducted by a commercial finite element software package COMSOL Multiphysics 5.6. IEHVG and IENG models were established for numerical simulation analysis.

Heat conduction: Along with the previous report, the heat transfer model can be simplified as a semi-infinite medium for the Cartesian coordinate system. Considering the presence of water molecules in the capillary channel, the heat transfer in the porous structure can be calculated by the equation given below describe:

$$E_{in} = \rho C_p \frac{\partial T(x,t)}{\partial t} + \rho C_p v \cdot \nabla T(x,t) + \nabla[k \nabla T(x,t)] \tag{1}$$

Where the E_{in} represents the thermal energy input from the optical-thermal conversion; T(x, t) is the local temperature; x and t are the space vector and time, respectively, and are the volume fraction, mass density, and thermal capacity of doped polymer, ν, ρ, an d C_p are the fluid flow speed, liquid mass density and its thermal capacity, respectively. The numerical simulations are conducted by COMSOL Multiphysics under the steady analysis mode. To carry out a qualitative analysis, we assume that the temperature of the environment and water was set to 25 ºC (298.15 K). The relevant parameters of water directly came from the material library of COMSOL Multiphysics.

Brine transport: The numerical simulation of water transport in the IEHVG evaporation system was analyzed by processing a Multiphysics situation coupled with the Laminar Flow Module and Fluid Heat Transfer Module. Meanwhile, the non-isothermal flow for Multiphysics coupling is considered. In order to clearly reveal the fluid motion patterns in the middle-layer and top-layer of the IEHVG, a cross-section 2D model was constructed, which corresponds to the actual dimensions of the IEHVG and IENG. The brine transport process could be illustrated by solving the following equations:

Laminar flow analysis:

$$\rho\frac{\partial_u}{\partial_t}+\rho(\mathbf{u}\cdot\nabla)\mathbf{u}=\nabla\cdot[-p\mathbf{I}+\mathbf{K}]+\rho g \quad (2)$$

$$\frac{\partial_\rho}{\partial_t}+\rho\nabla\cdot(\mathbf{u})=0 \quad (3)$$

$$\mathbf{K}=\mu\cdot(\nabla\mathbf{u}+(\nabla\mathbf{u})^T) \quad (4)$$

Fluid heat transfer analysis:

$$Q=d_z\rho C_p\frac{\partial T}{\partial t}+d_z\rho C_p\mathbf{u}\cdot\nabla T+\nabla\cdot\mathbf{q} \quad (5)$$

$$\boldsymbol{q} = -d_z k \nabla T \qquad (6)$$

where **u** represents the velocity field (m s^{-1}), both in laminar flow and heat transfer, ρ is the water density (kg m^{-3}), p is the pressure (Pa), **I** is the constitutive relation coefficient, and **K** is the water viscosity. μ is denoted as the dynamic viscosity, ϱ w is an automatic wall distance parameter; C_p is the water capacity at constant pressure (J kg^{-1} K^{-1}); **q** is the conductive heat flux (W m^{-2}) and g is the gravity (N).

Salt ions concentration distribution: The salinity increases because of the water loss during evaporation. Therefore, we carried out the simulation according to the water content (w m). The brine transport in the evaporator is expressed by:

$$\nabla \cdot (\rho_w \mu_{wc} + \rho_w \mu_{wd}) = g_{evap} M_w \qquad (7)$$

where μ_{wc} is the convection velocity ($\rho_w \nabla_{uw} \nabla_{wm}$) and μ_{wd} is the diffusion velocity ($D_w \nabla_{wm}$, D_w is the effective diffusion coefficient). M_w is the molar mass of water. Among them, the μ_{wc} is equal to the brine transport velocity, and μ_{wd} is related to temperature, porosity, and water saturation. Therefore, the result of the salinity is w_s (w_s=1-w_w). The boundary that contacts with water was set as the mass fraction of water (0.9, 0.85, 0.8, and 0.75).

Note S2. Materials fabrication

Fabrication of Ti_3C_2Tx MXene: 1 g of Ti_3AlC_2 was etched by a mixture of 1 g LiF and 20 mL 9 m HCL solution in a polytetrafluoroethylene bottle and then kept at 35 °C with continuous stirring for 24 h. Afterwards, the suspension was centrifuged (3500 rpm) and rinsed with distilled water for several times until the pH was higher than 5.5.

The obtained precipitate was further dispersed into 100 mL of deionized water, and under the protection of N_2 atmosphere, the ice water bath was ultrasonic for 1 h. The precipitates were collected by centrifugation at 8000 rpm for 10 min. The precipitates were dispersed into anhydrous ethanol and sonicated for 0.5 h under the protection of N_2 atmosphere. The supernatant was collected at 8000 rpm for 10 min. Ti_3C_2Tx nanosheets were obtained by freezing and drying the supernatant.

Fabrication of GQDs: Typically, 0.06 g of glucose was dissolved into 60 mL deionized water with constant stirring. Subsequently, the obtained mixed solution was transferred into a Teflon-lined stainless steel autoclave (100 mL) and heated at 150 °C for 10 h. For further purification of GQDs, the resulting solution was dialyzed in a dialysis bag (retained molecular weight: 1000 Da) for 48 h. The dialyzed GQDs solution was freeze dried at -60 °C for 48 h to obtain GQDs powder.

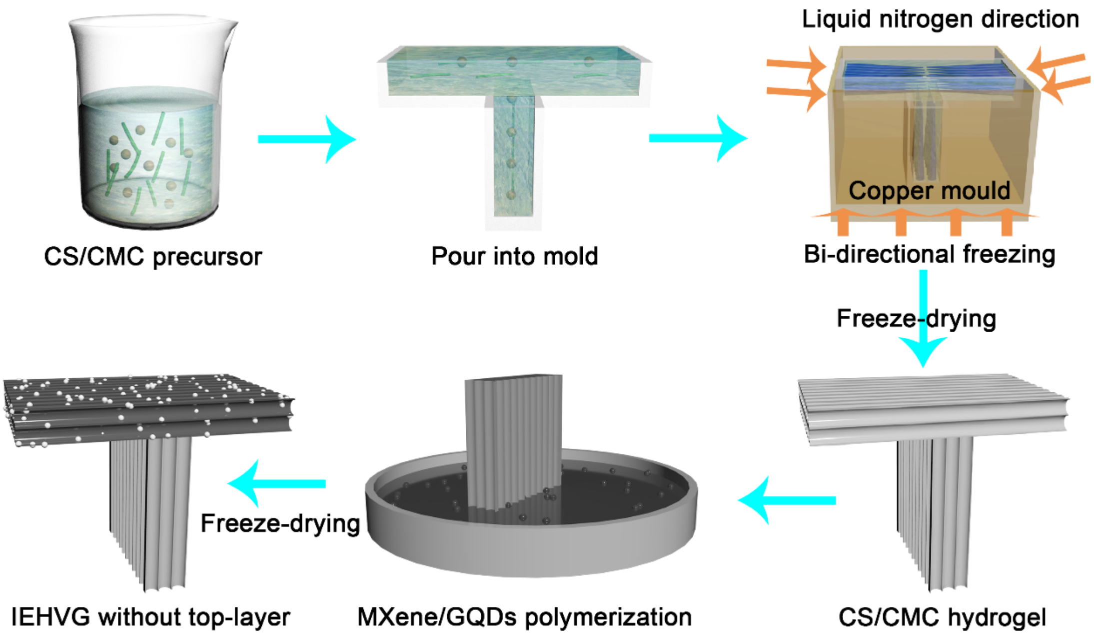

Figure S1. Schematic diagram of the IEHVG preparation process, including hydrogel precursor solution, injection process, bi-directional freezing, freeze-drying, and MXene/GQDs self-polymerization process.

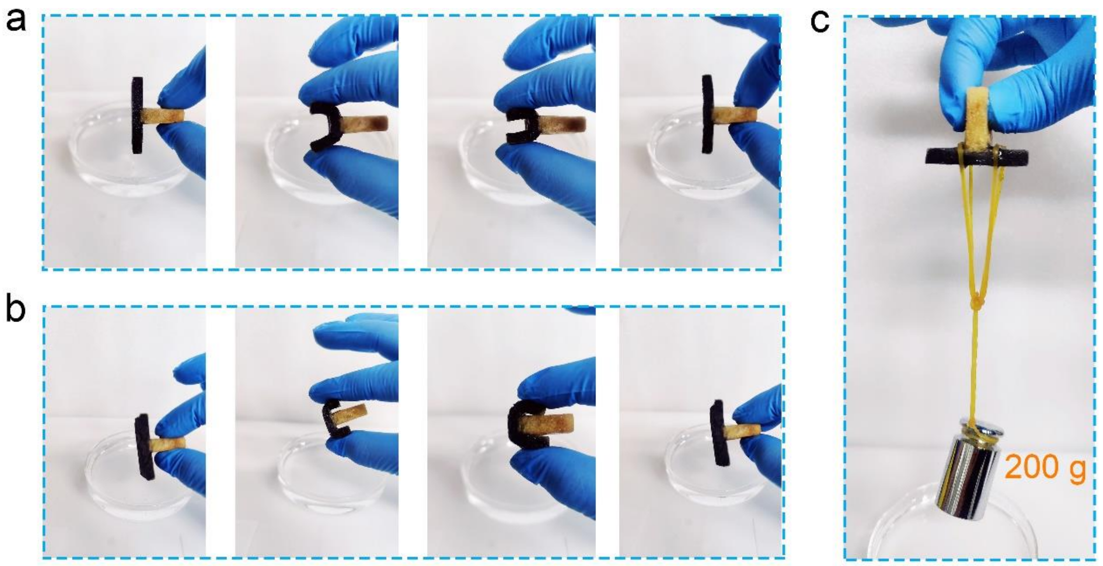

Figure S2. Mechanical properties testing of IEHVG.

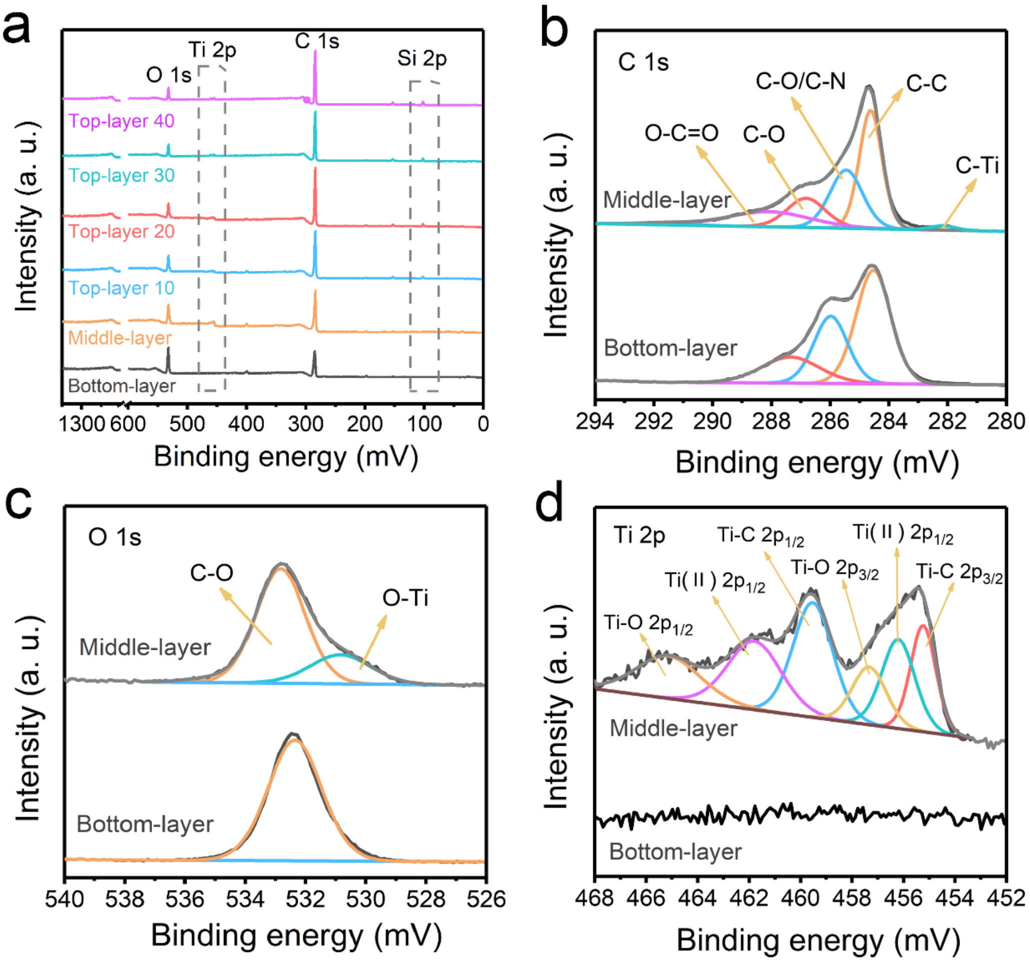

Figure S3. Hierarchical functionalization of IEHVG, **a** XPS spectra of bottom, middle, and top-layer, **b-d** high-resolution C, O, and Ti spectra of bottom and middle-layer.

The surface elemental composition and chemical state of the IEHVG layers were analyzed using X-ray photoelectron spectroscopy (XPS). As shown in Fig. 2a, the C and O signals in the bottom-layer, the added Ti signal in the middle-layer, and the Si signal in the top-layer can be clearly identified. Compared with the bottom-layer, due to the GQDs/Ti_3C_2Tx composite in the middle-layer, the deconvoluted C 1s spectrum was observed in the spectra consisting of five peaks located at the binding energies of 282.4, 284.8, 286.0, 286.7, and 288.5 eV (Fig. 2b), which corresponded to the C-Ti, C-C, C-O/C-N, C-O, and O-C=O groups, respectively, confirming the successful introduction and interaction of MXene with GQDs. The high-resolution O 1s spectrum can be decomposed into two peaks at 530.2, 532.7 eV, which are assigned to Ti-O and C-O configurations, respectively (Fig. 2c). For O 1s spectrum of middle-layer, there is no additional oxidation peak at 531 eV, confirming that no significant surface oxidation has occurred. Moreover, the high-resolution Ti 2p spectrum consists of three two-particles centered at 455.2/459.3, 456.1/461.7, and 457.4/463.2 eV, which correspond to the Ti - C, Ti(II), and Ti - O signals, respectively.

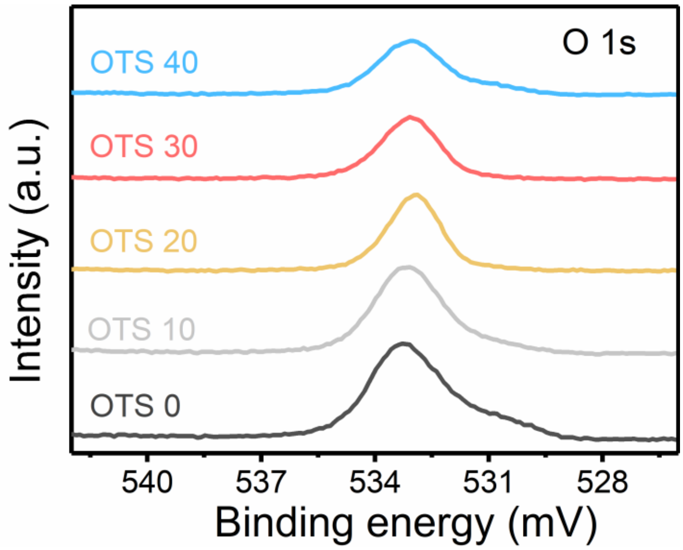

Figure S4. High-resolution O 1s spectra of regionalized top-layer modified by different OTS cycles.

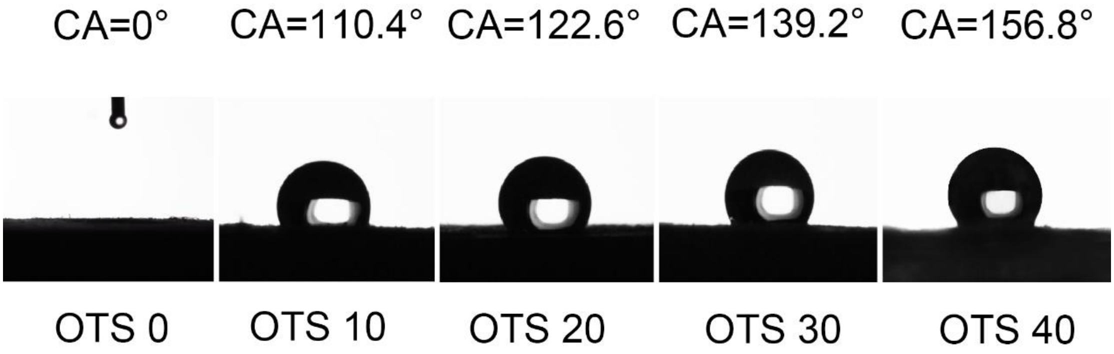

Figure S5. Water contact angle of regionalized top-layer modified by different OTS cycles.

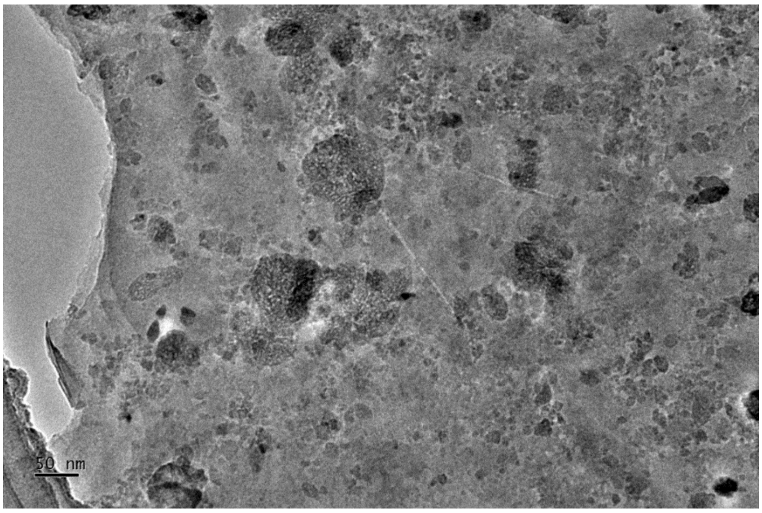

Figure S6. TEM image of the MXene/GQDs composite on the middle-layer.

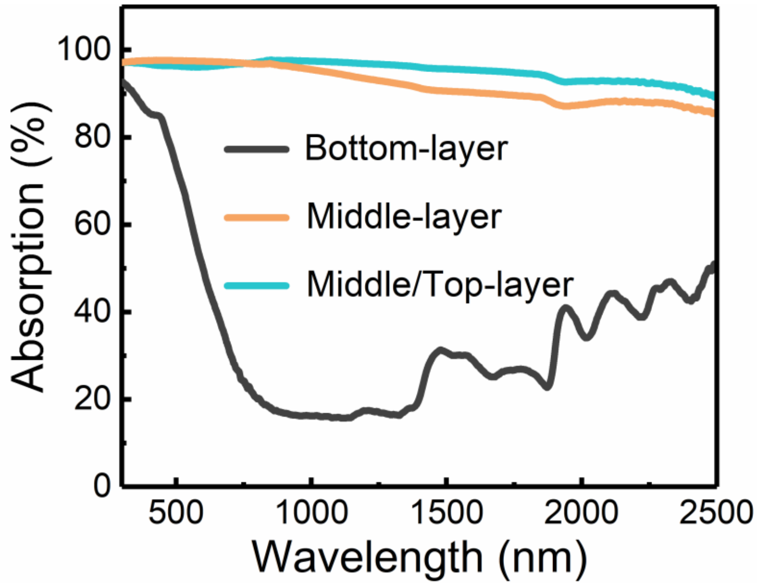

Figure S7. Solar absorption spectra of the IEHVG in the wavelength range of 200–2500 nm.

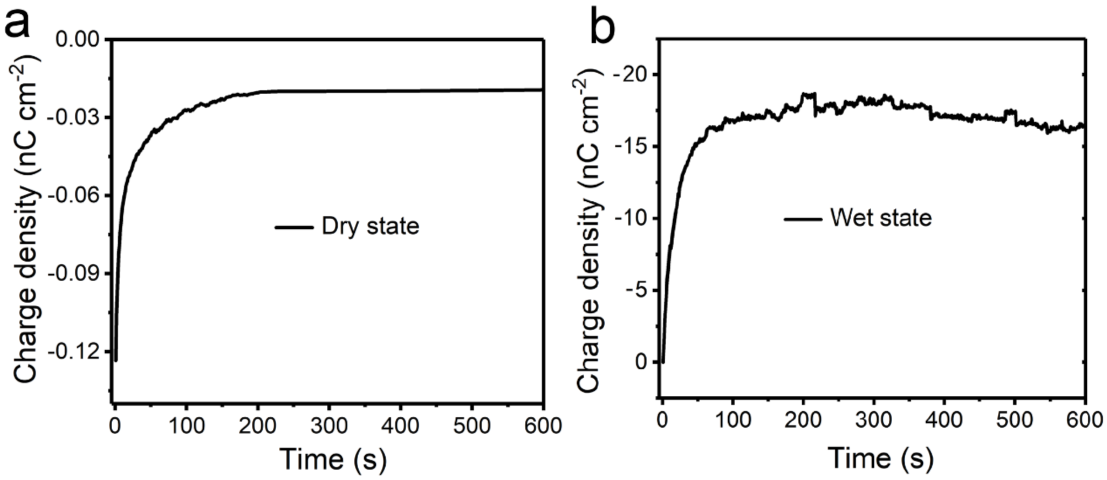

Figure S8. a Surface charge distribution of the dried IEHVG. **b** Surface charge distribution of the wet IEHVG.

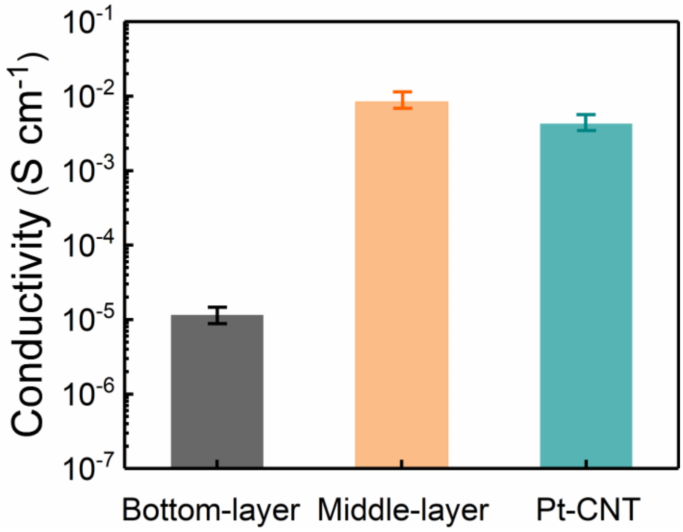

Figure S9. Electrical conductivity of bottom-layer, middle-layer, and between PT-CNT electrodes

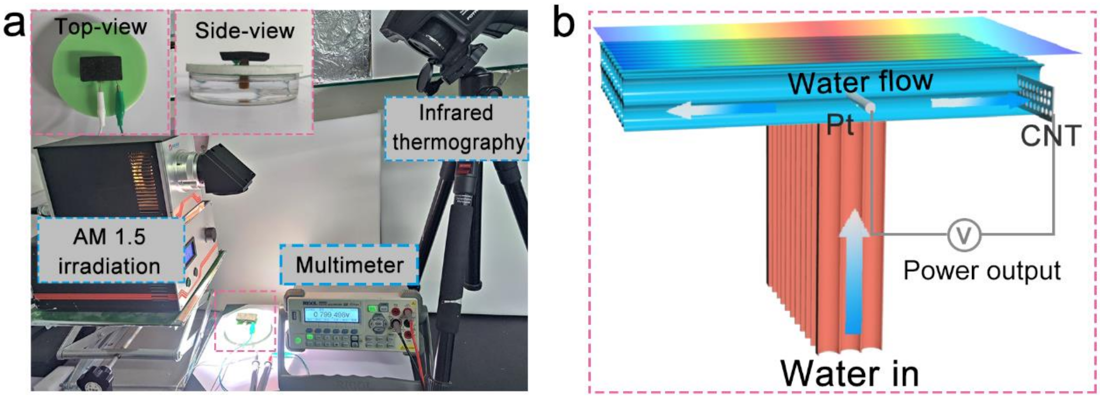

Figure S10. Optical photographs and schematic of the IEHVG system during the test process under simulated solar irradiation.

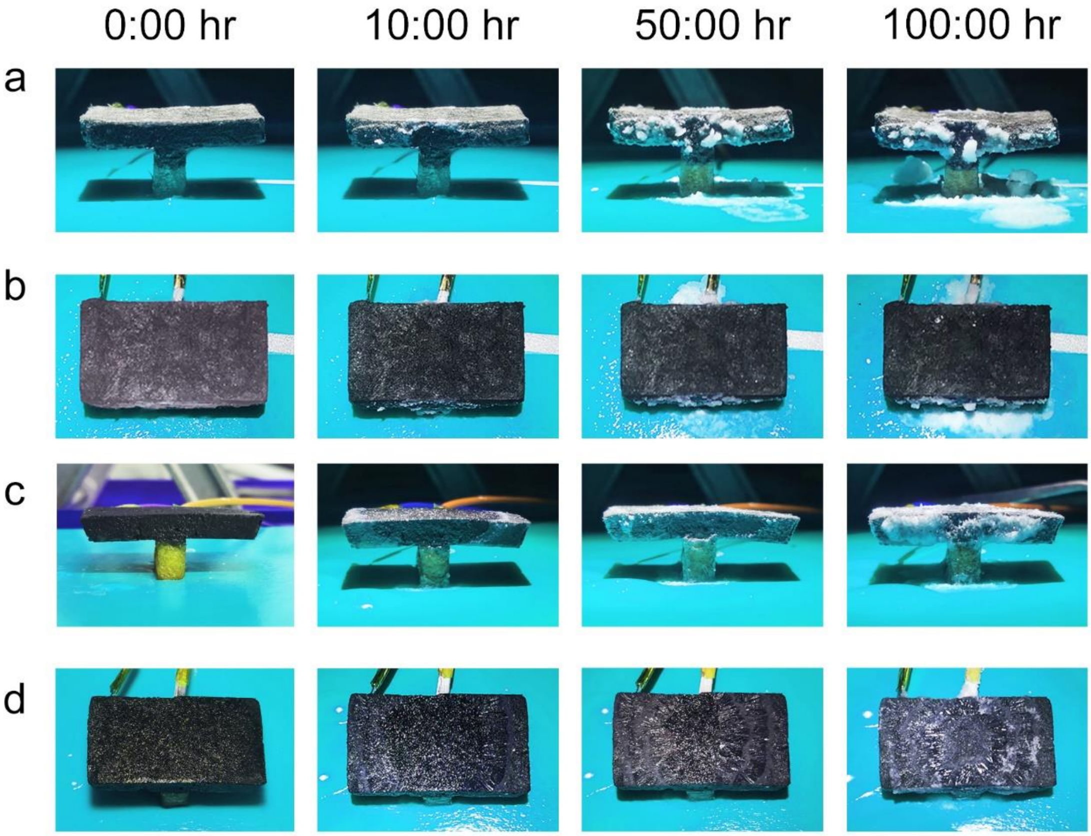

Figure S11. Optical photographs of salt crystallization at IEHVG in seawater continuously for 100 h irradiated under 1 sun, **a** side-view, and **b** top-view. Optical photographs of salt crystallization at IENG in seawater continuously for 100 h irradiated under 1 sun, **c** side-view, and **d** top-view.

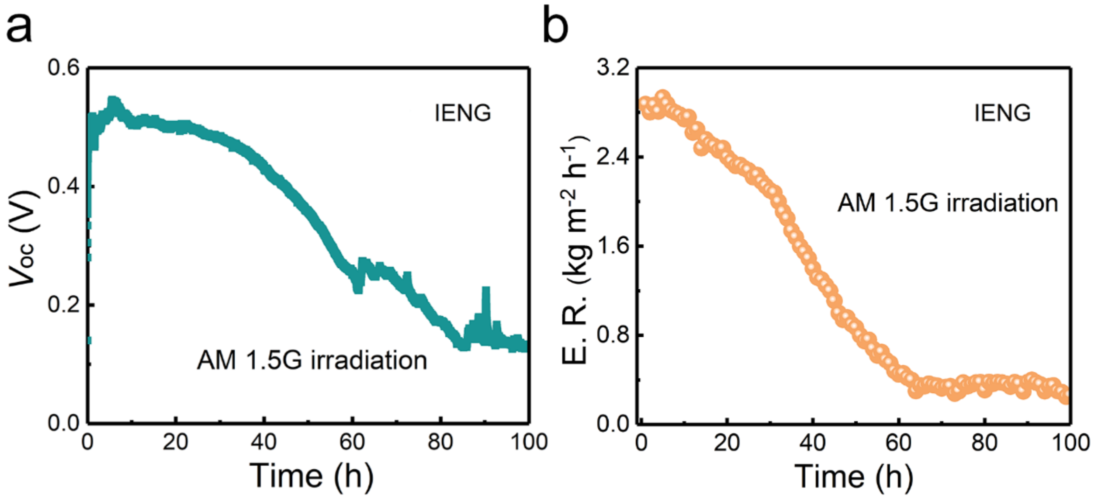

Figure S12. Voc and E. R. of IENG in seawater continuously for 100 h irradiated under 1 sun.

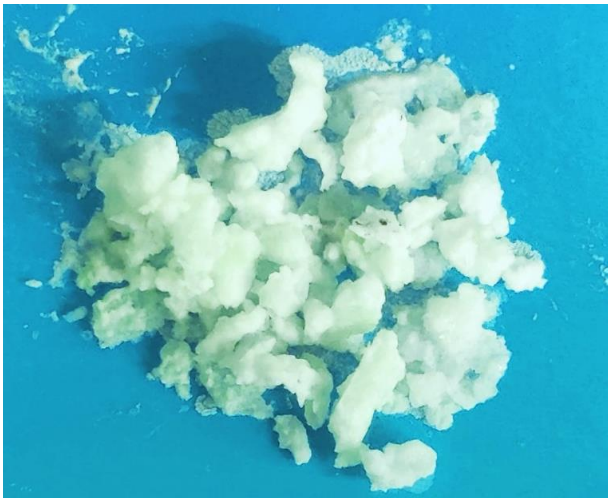

Figure S13. Salt crystals collected from seawater continuously for 100 h irradiated under AM 1.5 irradiation.

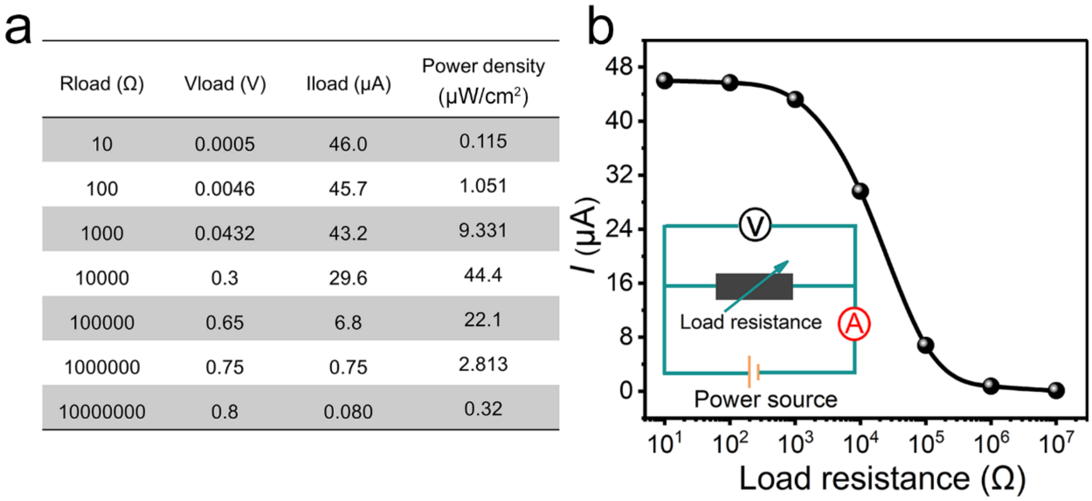

Rload (Ω)	Vload (V)	Iload (μA)	Power density (μW/cm^2)
10	0.0005	46.0	0.115
100	0.0046	45.7	1.051
1000	0.0432	43.2	9.331
10000	0.3	29.6	44.4
100000	0.65	6.8	22.1
1000000	0.75	0.75	2.813
10000000	0.8	0.080	0.32

Figure S14. a Output voltage, current, and power density of the IEHVG as functions of the load resistance. **b** Inset is the corresponding circuit schematic.

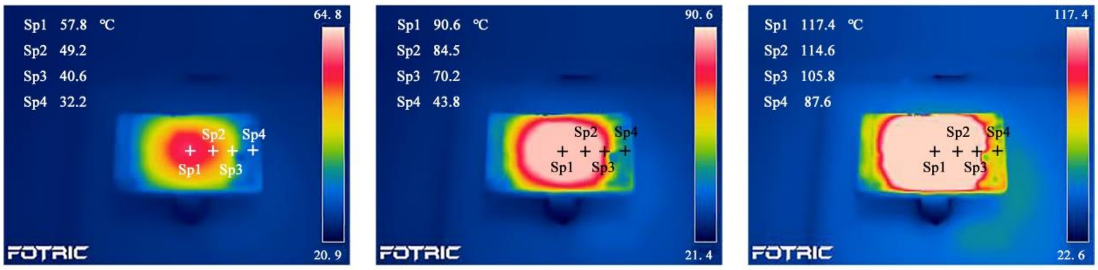

IEBNG under 500 W/m^2 1000 W/m^2 2000 W/m^2

Figure S15. Temperature on the surface of IEHVG recorded by infrared camera under different solar intensity.

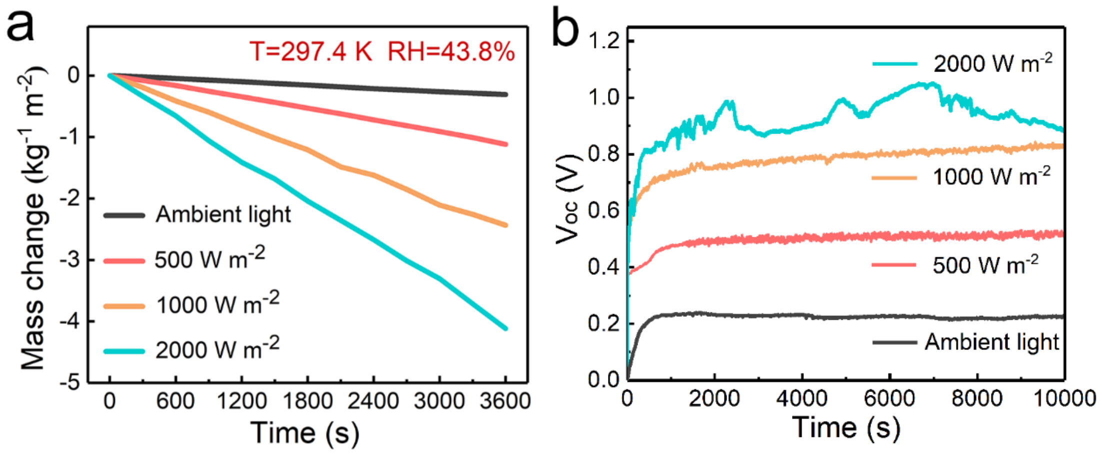

Figure S16. a Mass change and **b** V_{oc} of IEHVG under different solar intensity.

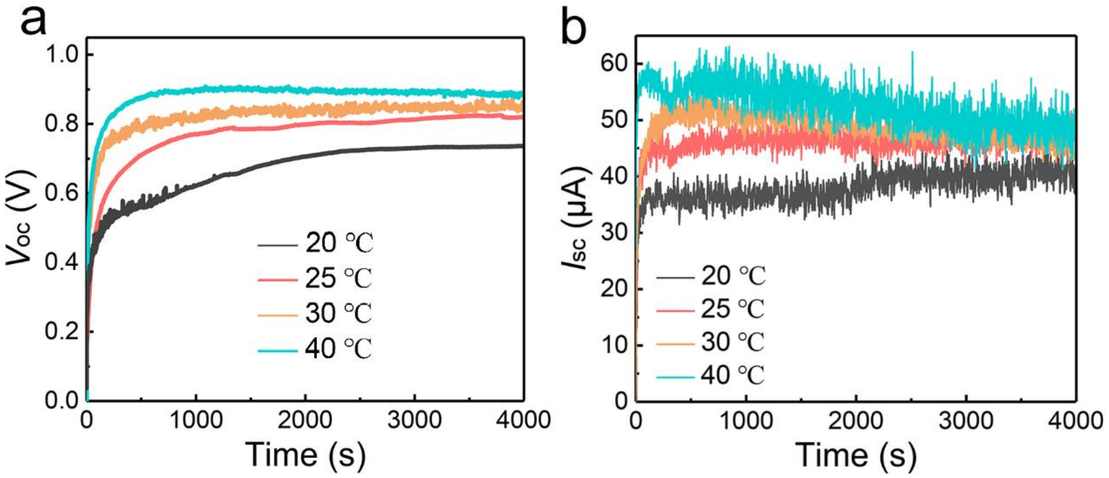

Figure S17. a The V_{oc}, and **b** I_{sc} of IEHVG with different water temperature.

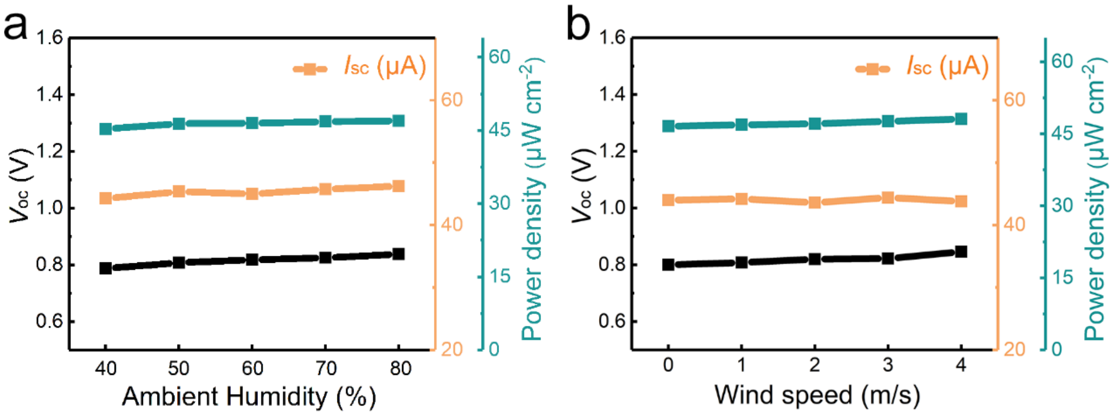

Figure S18. The V_{oc}, I_{sc}, and power density of the IEHVG under **a** different ambient humidity, and **b** wind speed.

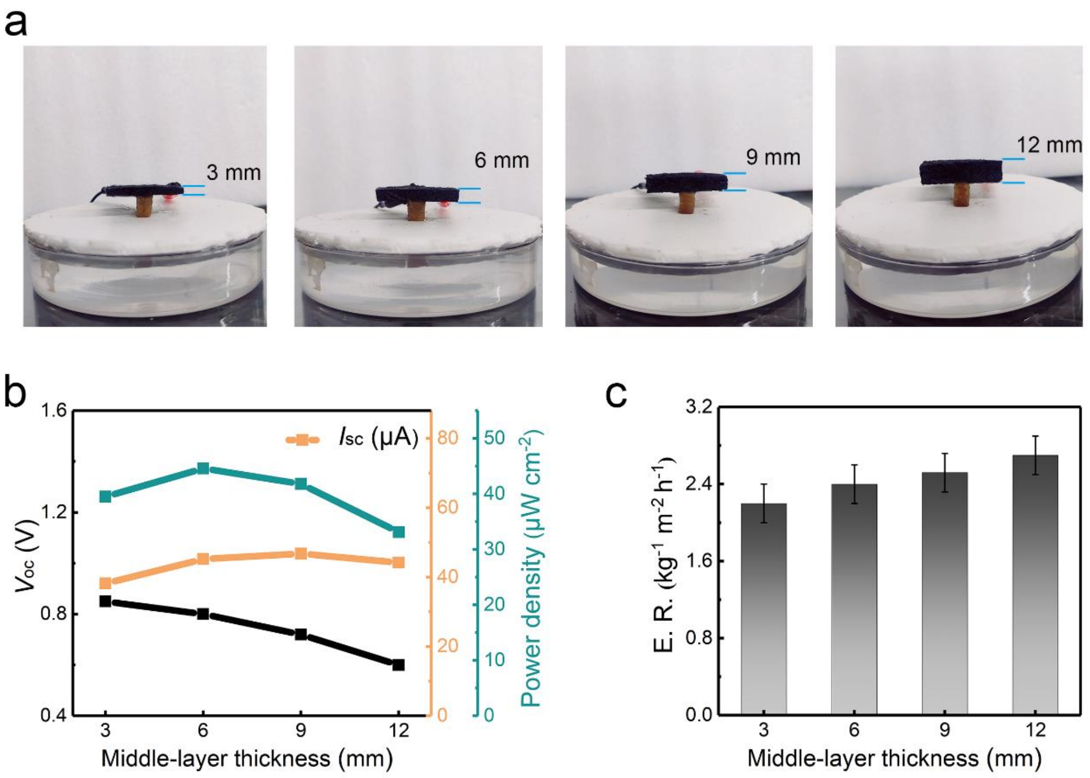

Figure S19. **a** The optical photographs, **b** power generation, and **c** water evaporation performance of IEHVGs with different thicknesses of middle-layers.

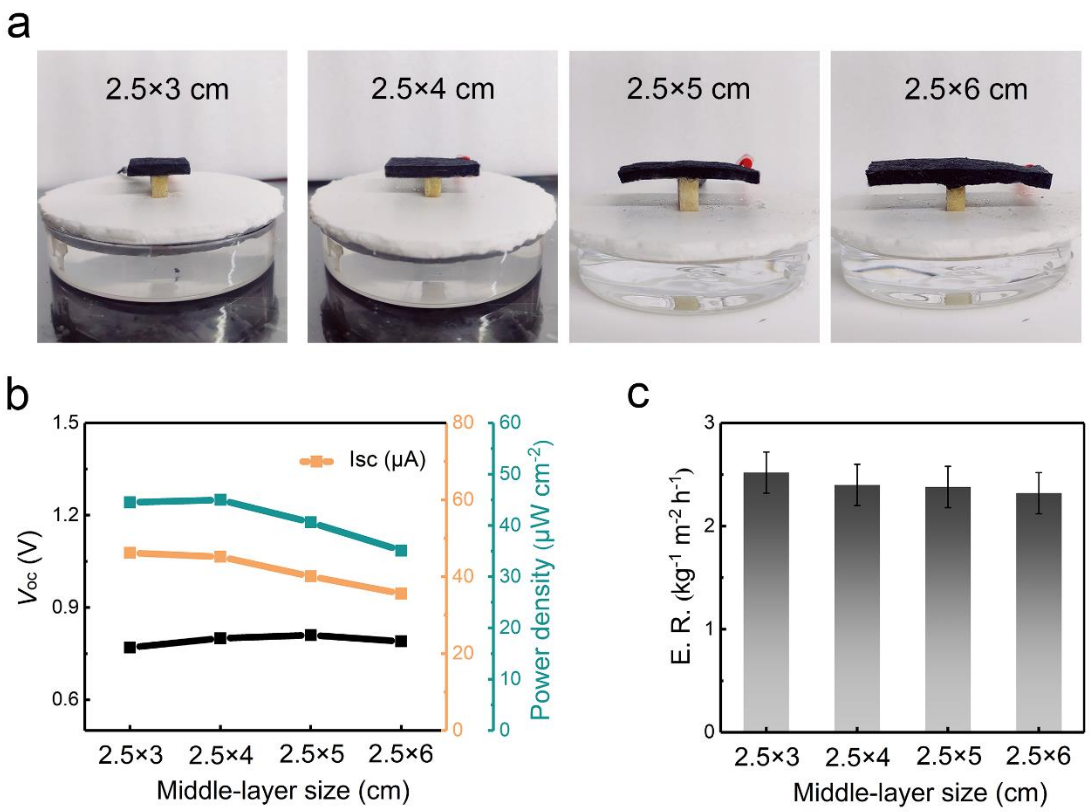

Figure S20. **a** The optical photographs, **b** power generation, and **c** water evaporation performance of IEHVGs with different surface area of middle-layers.

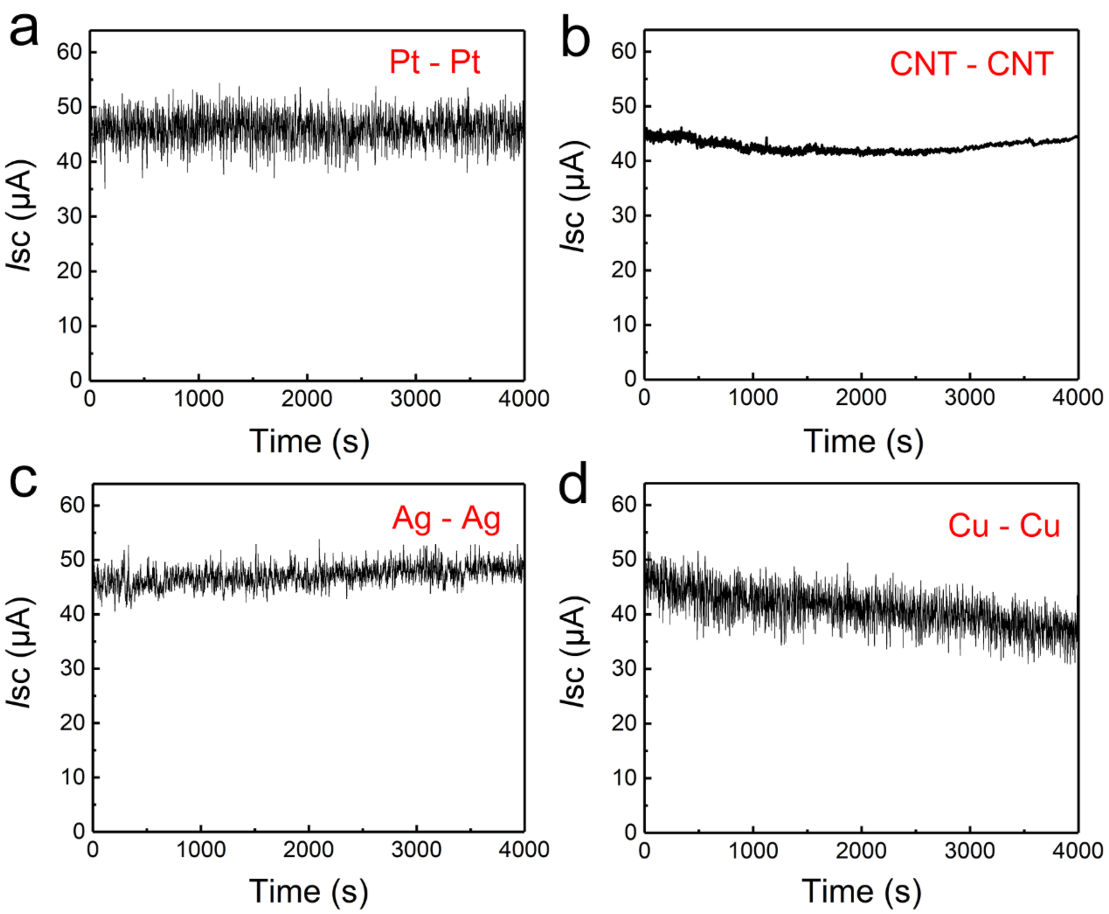

Figure S21. The I_{sc} of IEHVGs using different electrodes. **a** Pt-Pt electrode. **b** CNT-CNT electrode. **c** Ag-Ag electrode. **d** Cu-Cu electrode.

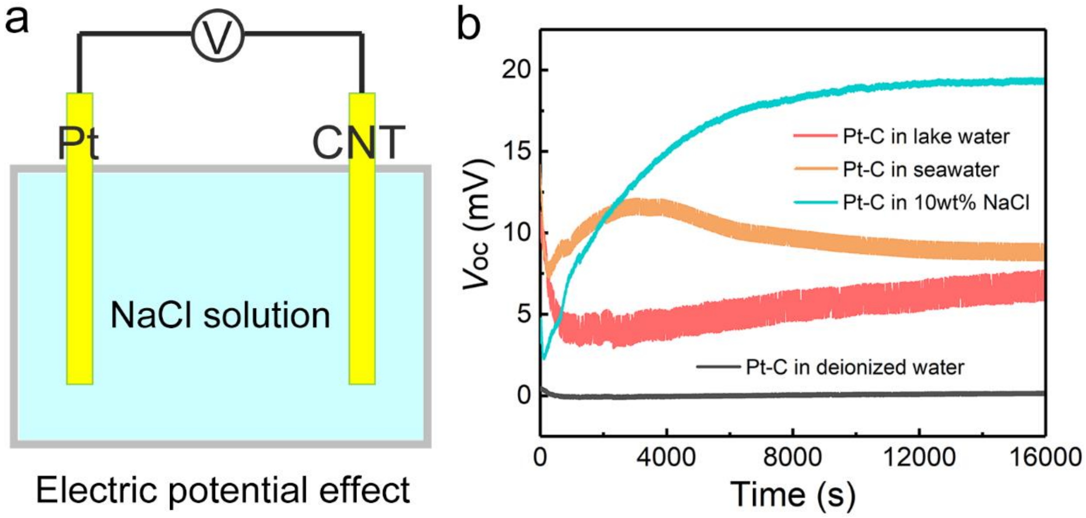

Figure S22. a Schematic diagram of the electric potential effect of the electrode in NaCl solution. **b** V_{oc} variation of Pt-CNT electrode in different solutions.

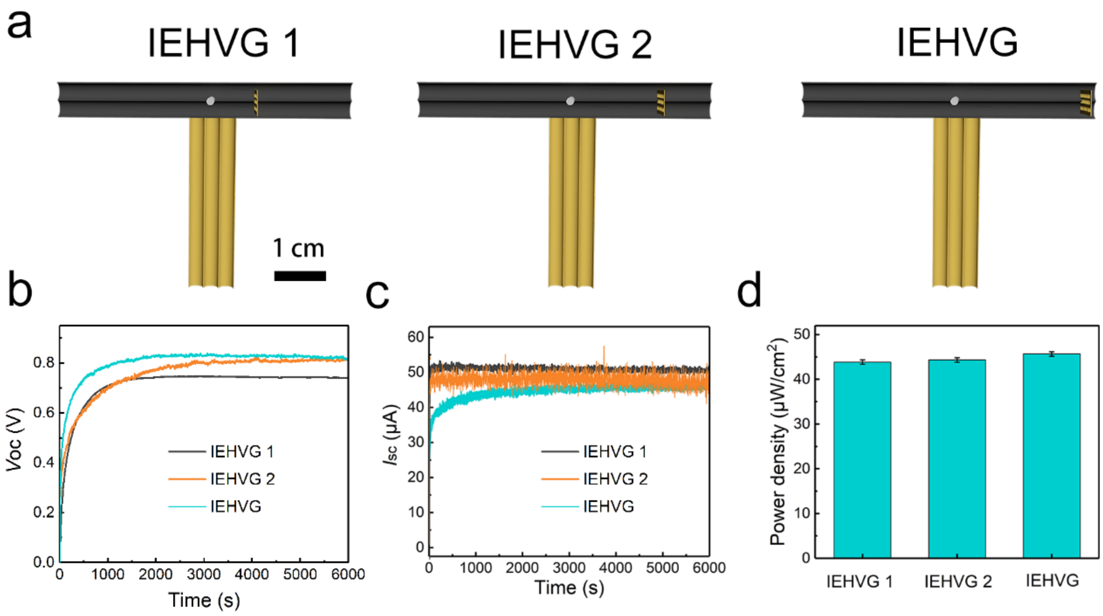

Figure S23. The output performance of IEHVGs with different inter-electrode distances.

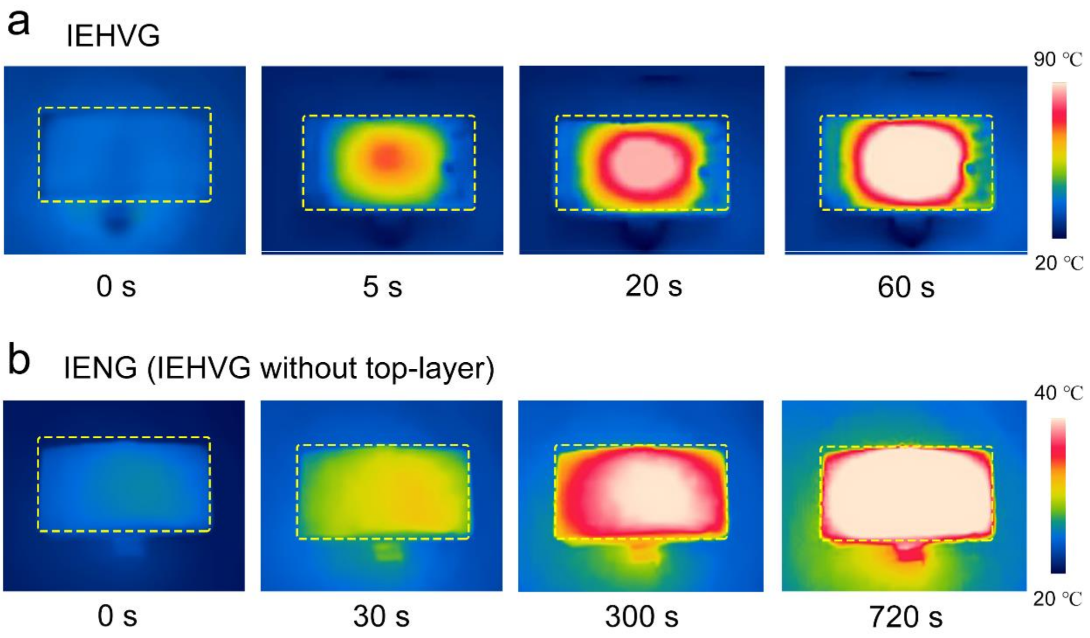

Figure S24. Temperature changes on the surface of **a** IEHVG, and **b** IENG recorded by infrared camera under 1.0 kW m^{-2} solar intensity.

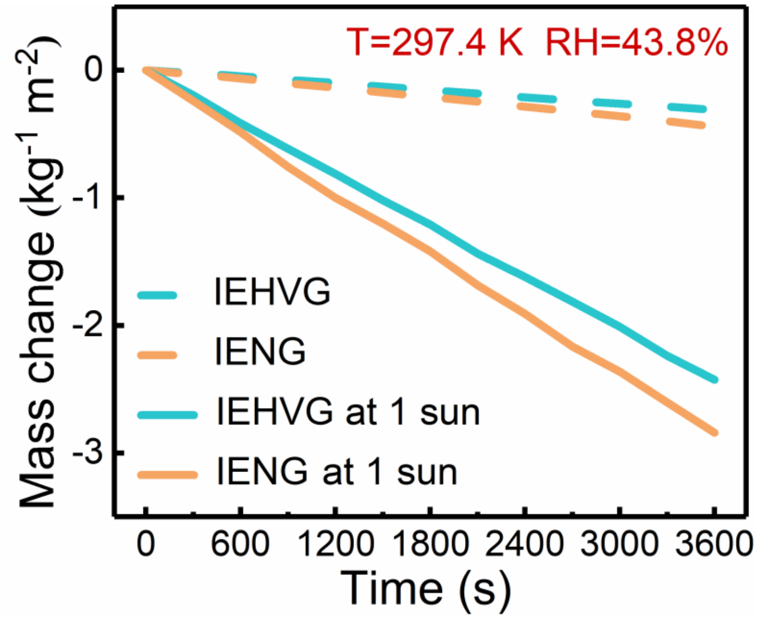

Figure S25. Water evaporation mass loss from IEHVG and IENG under natural light and 1 sun.

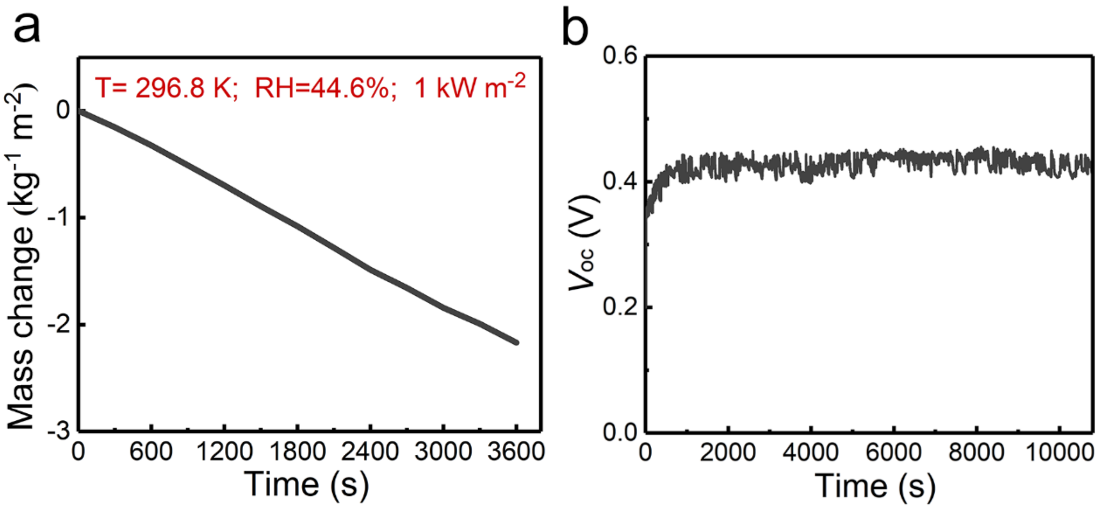

Figure S26. Water evaporation mass loss and V_{oc} from IEHVG with non-gradient hydrophobic coating under 1 sun.

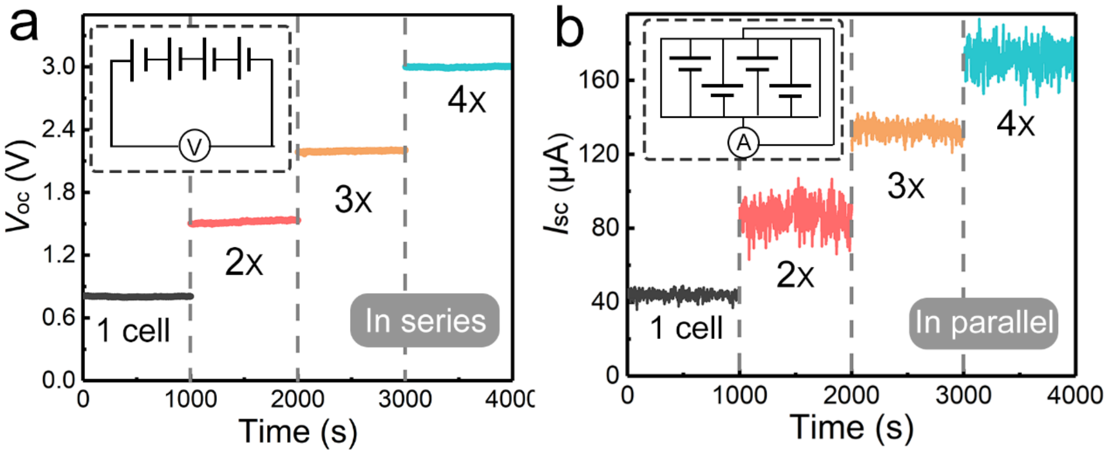

Figure S27. a Voltage output of the IEHVG with increasing numbers of device units in series. The inset presents a circuit diagram. **b** Current output of the IEHVG with increasing numbers of device units in parallel. The inset presents a circuit diagram.

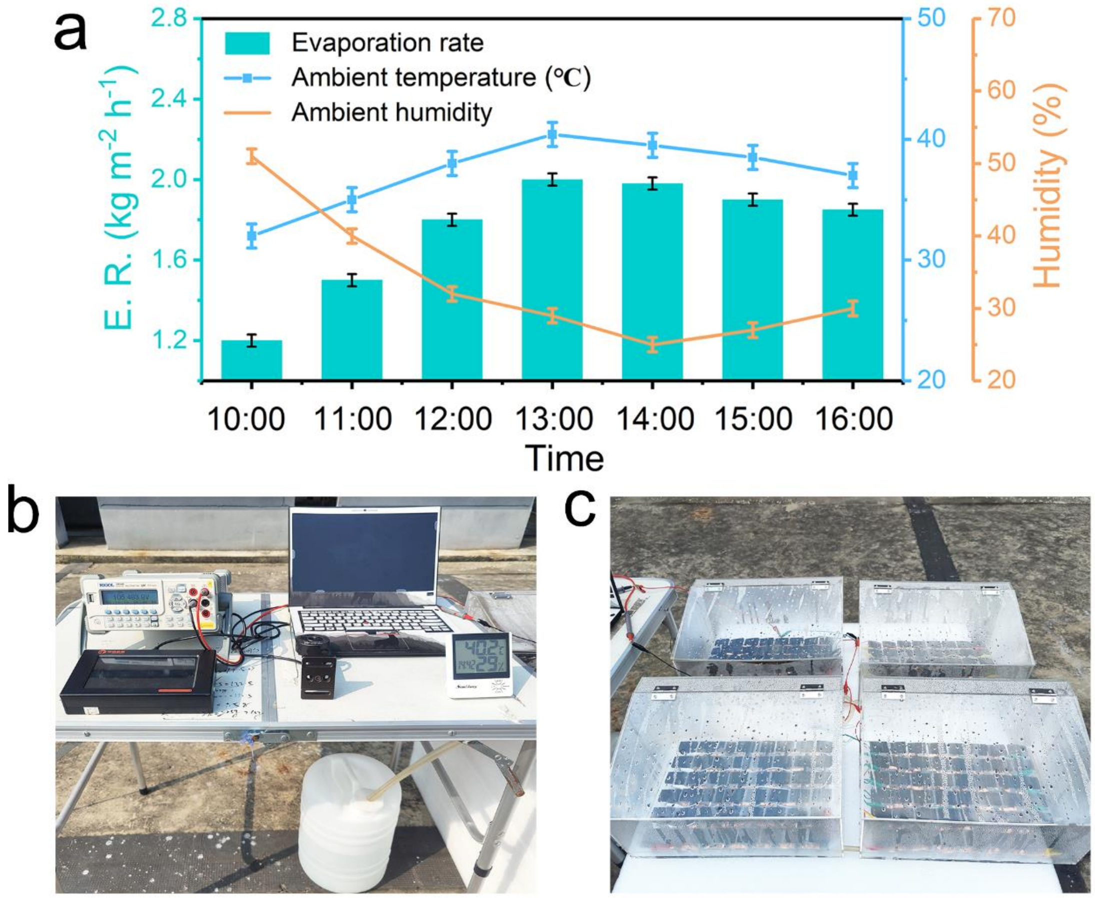

Figure S28. **a** The evaporation rate, ambient temperature, and humidity detection for outdoor experiments. **b** Optical photographs of the water- electricity cogeneration plant detection and collection system. **c** Optical photographs of the water-electricity cogeneration plant in real-time operating conditions.

Table S1: Comparison of the power generation performance of IEHVG with other reported HVGs.

Reference	HVGs	V_{oc}/V	I_{sc}/Current density	Power density/ μW cm^{-2}
Ref 8	SiNWs	0.4	55 μA cm^{-2}	6
Ref 9	SiNWs/PEDOT:PSS	0.55	22 μA cm^{-2}	10
Ref 10	Microbial biofilms	0.45	1.5 μA	1
Ref 13	Hydrovoltaic wood	0.14	7 μA	1.35
Ref 15	AgInZnS	0.75	4.2 μA	0.8
Ref 27	PNCSi-HD	0.45	10.2 μA	1.42
Ref 28	IENG	0.432	64.2 μA cm^{-2}	11.8
Ref 29	PN-MEG	0.65	2.9 μA	38.88
Ref 38	SSEG	0.78	7.5 μA	0.7
This work	IEHVG	0.8	46 μA	45.6